

Journal of Materials Chemistry A

Materials for energy and sustainability

Accepted Manuscript

This article can be cited before page numbers have been issued, to do this please use: X. Liu, Z. Li, Z. Du, C. Wang, H. Zhang, S. Luo and S. Zhang, *J. Mater. Chem. A*, 2025, DOI: 10.1039/D5TA04814A.



This is an Accepted Manuscript, which has been through the Royal Society of Chemistry peer review process and has been accepted for publication.

Accepted Manuscripts are published online shortly after acceptance, before technical editing, formatting and proof reading. Using this free service, authors can make their results available to the community, in citable form, before we publish the edited article. We will replace this Accepted Manuscript with the edited and formatted Advance Article as soon as it is available.

You can find more information about Accepted Manuscripts in the [Information for Authors](#).

Please note that technical editing may introduce minor changes to the text and/or graphics, which may alter content. The journal's standard [Terms & Conditions](#) and the [Ethical guidelines](#) still apply. In no event shall the Royal Society of Chemistry be held responsible for any errors or omissions in this Accepted Manuscript or any consequences arising from the use of any information it contains.

Emerging innovations in polymeric hollow fiber membranes for sustainable natural gas valorization

Xing Liu ^{a,b,c}, Zhenyuan Li ^b, Zanchun Du ^b, Can Wang ^b, Haitao Zhang ^b, Shuangjiang Luo ^{a,b*}, Suojia Zhang ^{b*}

^a Shanxi-Zheda Institute of Advanced Materials and Chemical Engineering, Taiyuan, 030000, China

^b CAS Key Laboratory of Green Process and Engineering, Beijing Key Laboratory of Solid State Battery and Energy Storage Process, State Key Laboratory of Mesoscience and Engineering, Institute of Process Engineering, Chinese Academy of Sciences, Beijing 100190, China

^c University of Chinese Academy of Sciences, Beijing 101408, China

Email: sjluo@ipe.ac.cn (S. Luo), sjzhang@ipe.ac.cn (S. Zhang)

Abstract: Polymeric hollow fiber membranes (HFMs) have emerged as a transformative technology for sustainable natural gas valorization, offering energy-efficient solutions for acid gas (CO₂, H₂S) removal and helium (He) recovery. This review highlights recent advancements in material design, fabrication strategies, and performance optimization of HFMs tailored for aggressive natural gas feeds. Key innovations include the engineering of polymer structures, coupled with asymmetric architectures (dual-layer, thin-film composites), which overcome the intrinsic permeance-selectivity trade-off, achieving industrially relevant permeance and selectivities. Advanced mitigation strategies for membrane aging and plasticization, including crosslinking and siloxane hybridization, are elucidated at the molecular level, demonstrating enhanced stability under high-pressure conditions. Furthermore, breakthroughs in processing techniques (e.g., co-extrusion spinning, interfacial polymerization) enable the fabrication of ultra-thin selective layers with defect-free interfaces. Emerging tools like machine learning and green solvents are also discussed as enablers of scalable and eco-friendly manufacturing. This work provides a comprehensive roadmap for next-generation HFMs, bridging molecular design with



31 industrial deployment to advance decarbonization in energy systems. By addressing
32 critical challenges and future opportunities, this review aims to inspire further research
33 in high-performance membrane materials for sustainable natural gas processing.

34
35 **Keywords:** gas separation membranes, hollow fiber membranes, plasticization
36 resistance, physical aging suppression, natural gas upgrading



1 Introduction

Natural gas has emerged as a critical pillar in the global energy transition, offering a pragmatic balance between escalating energy demands and decarbonization imperatives.¹ Its combustion emits 40-50% less CO₂ per unit energy than coal and oil, coupled with higher calorific efficiency and negligible particulate emissions, positioning it as a transitional fuel toward net-zero goals.² Global consumption has surged from 14.56% of primary energy in 1965 to 23.30% today, with a projected 12% growth by 2030.³ However, raw natural gas is rarely pristine, containing corrosive impurities such as carbon dioxide (CO₂) and hydrogen sulfide (H₂S), which necessitate purification to meet pipeline specifications (<2% CO₂, <4 ppm H₂S) and mitigate infrastructure corrosion.^{4, 5} Concurrently, select reservoirs harbor helium (0.01-5%), a nonrenewable resource vital for semiconductors and magnetic resonance imaging technologies, yet conventional extraction methods falter at low-concentration (<0.1%) due to thermodynamic inefficiencies.⁶⁻⁹

Current separation technologies face sustainability trade-offs. Solvent absorption, though effective for bulk CO₂ and H₂S removal, consumes 30-40% of processing energy for solvent regeneration and generates corrosive waste.¹⁰ Cryogenic distillation, while achieving high helium purity (99.999%), incurs prohibitive costs for lean reserves (<0.1% He) due to energy-intensive liquefaction.¹¹ These limitations underscore the urgency for energy-efficient alternatives. Membrane-based separation has gained traction as a low-carbon solution, offering continuous operation without chemical additives and modular scalability suited to decentralized gas fields.^{12, 13} Among membrane configurations, hollow fiber modules dominate industrial adoption due to their intrinsic self-supporting architecture, unmatched packing densities (up to 10⁴ m² m⁻³), ease of scale-up, and superior mechanical resilience compared to spiral-wound and plate-and-frame modules.¹⁴

The evolution of polymeric hollow fiber membranes (HFMs) for natural gas treatment traces back to the 1970s with asymmetric cellulose acetate HFMs, achieving



CO₂/CH₄ selectivity of 12-15 but succumbing to plasticization at CO₂ partial pressures >5 bar (Fig. 1).^{10, 15, 16} A paradigm shift occurred in 1994 when polyimide-based HFMs (Medal, Air Liquide) doubled CO₂/CH₄ selectivity to 20-25 while resisting hydrocarbon-induced plasticization.¹⁶ By 2020, HFM systems accounted for 18% of global natural gas processing capacity, with over 500 installations treating >200 billion m³ annually. These industrial deployments now demonstrate high-efficiency decarbonization, resource valorization, and extreme-condition resilience. For instance, ADNOC's Habshan facility achieves 99% CO₂ removal from 10 MMSCFD streams with <2% CH₄ loss, Evonik's helium-selective HFMs (He/CH₄ selectivity >150) enable economic extraction from sources containing <2% He, Air Products' methane recovery modules, and UBE's H₂S-tolerant polyimide HFMs handle >30,000 ppm H₂S streams without performance decay. These field-proven capabilities establish HFMs as essential components for achieving net-zero emissions targets, specifically in carbon capture applications and helium recovery from unconventional resources. However, persistent challenges associated with plasticization and physical aging phenomena necessitate fundamental innovations in advanced membrane materials.

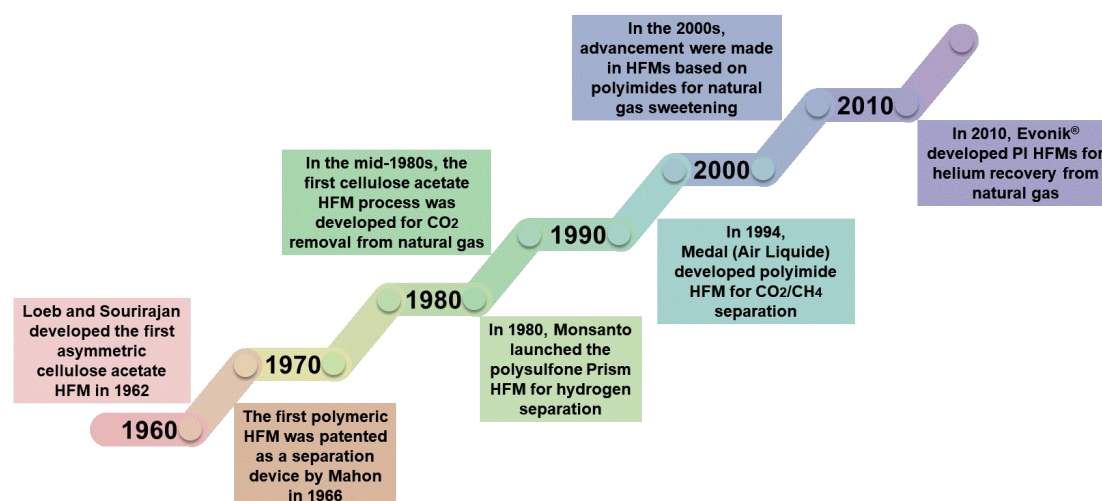


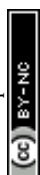
Fig. 1 Milestones in commercial HFM development for natural gas treatment.

Despite these advances, existing reviews inadequately address the material-process-performance interplay specific to natural gas treatment scenarios. Prior works predominantly focused on generic fabrication techniques or broad gas separation



applications.¹⁷⁻²³ For instance, Chung et al. (2012) detailed phase-inversion principles for HFM formation, with applications spanning CO₂ capture, H₂ production, and desalination.²⁴ While Othman et al. (2018) pioneered the analysis of dual-layer HFMs, emphasizing coextrusion fabrication and comparative advantages over single-layer designs.²⁵ Kujawski et al. (2020) systematically categorized asymmetric, thin-film composite, and mixed-matrix HFMs, correlating transport mechanisms with performance,¹⁷ and Yong et al. (2021) advanced theoretical frameworks linking spinning parameters to membrane morphology and gas separation efficiency in applications like air separation and propylene/propane splitting.²⁶ Recent works, such as Imtiaz et al. (2022) on braid-reinforced HFMs and Lau et al. (2024) on surface modification techniques, further expanded the technical repertoire.^{15, 27} However, these studies lack dedicated focus on natural gas treatment, particularly in addressing two critical challenges: (1) the intrinsic relationship between the hierarchical structure of HFMs and their gas separation performance remains unclear, particularly regarding natural gas sweetening under complex gas source conditions and helium extraction from low-concentration sources, and (2) the microscopic mechanisms of aging in polymeric HFMs, along with their plasticization behaviors and anti-plasticization strategies under high CO₂ and light/heavy hydrocarbon exposure, require further elucidation.

This review bridges these gaps by providing a comprehensive analysis of HFMs tailored for natural gas treatment. We begin by elucidating the configuration of asymmetric HFMs and the fundamental mechanism governing gas transport, followed by a critical evaluation of fabrication methods (e.g., co-extrusion, dip-coating, and interfacial polymerization) and post-modification strategies. Subsequently, we critically analyze advanced polymer materials, including cellulose acetate, polysulfone, polyimides, thermally rearranged polymer, and carbon molecular sieves, specifically engineered for acid gas removal and helium recovery. Challenges such as nanoporous transition layer collapse, physical aging, and plasticization are examined alongside



emerging solutions like crosslinking and hybrid matrix designs. Finally, we propose a sustainability-driven roadmap for future research, emphasizing scalability, lifecycle assessment, and alignment with decarbonization goals (Fig. 2). By integrating material innovation with industrial practicality, this work advances HFM technology toward sustainable natural gas valorization.

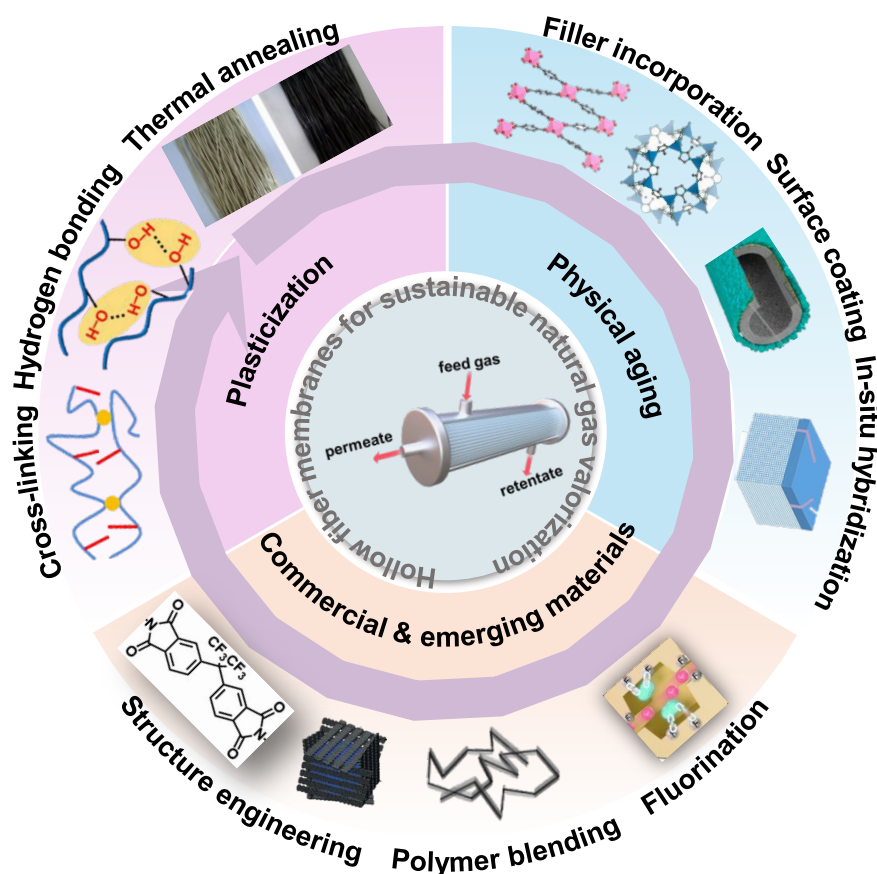


Fig 2. Schematic diagram of emerging innovations in polymeric hollow fiber membranes for sustainable natural gas valorization.

2 Fundamentals of gas permeation in hollow fiber membranes

Gas transport mechanisms in membranes depend critically on membrane microporosity and gas-material interactions.²⁸ The solution-diffusion mechanism prevails in polymeric membranes, where separation arises from differential dissolution and diffusion through transient free-volume elements (Fig. 3a). By contrast, pore-mediated mechanisms govern gas transport in porous membrane architectures (Fig. 3b), including molecular sieving via steric exclusion in micropores, surface diffusion driven



by adsorbed-phase transport, and limited-selectivity flows such as Knudsen or Poiseuille diffusion.²⁹ Crucially, polymeric HFMs primarily exploit solution-diffusion within their dense selective layers, while pore-based mechanisms dominate in nanostructured materials like polymer-derived carbon molecular sieves (CMS) or nanocomposites incorporating engineered nanoporous fillers.

An integrally asymmetric HFM achieves optimal separation performance through a carefully designed multilayer structure, as shown in Fig. 4a. The membrane consists of three fundamental layers: (1) a macroporous support layer (100-300 μm thick, 60-80% porosity) that provides mechanical stability while contributing less than 5% of total transport resistance; (2) a mesoporous transition layer (1-10 μm thick, 1-50 nm pore size) that serves two critical functions which gradually bridges the large pores of the support with the dense selective layer to prevent delamination, and regulates solvent exchange kinetics during phase inversion for facilitating formation of defect-free selective layer; (3) an ultrathin dense selective skin layer (10-1000 nm thick) where molecular sieving primarily occurs. Some advanced configurations may include additional protective coatings (e.g., 10-1000 nm silicone rubber) to heal surface defects, particularly for membranes operating under harsh conditions.¹³ This hierarchical architecture enables more than 95% of the separation to occur at the selective layer while maintaining excellent mechanical properties.³⁰

Gas permeation through the dense selective layer of polymeric HFMs normally follows the solution-diffusion mechanism. In this process, gas molecules first absorb onto the membrane high-pressure upstream surface, then diffuse through the polymer matrix via thermally activated jumps between transient free-volume elements driven by a concentration gradient and finally desorb into the low-pressure downstream side as permeate. The steady-state gas flux (Q_i) for component i is expressed as:³¹

$$Q_i = \frac{P_i A \Delta P}{L} = \frac{\Delta P}{\left(\frac{L}{P_i A}\right)}$$

where P_i is permeability (Barrer, 1 Barrer = $10^{-10} \text{ cm}^3 \text{ (STP) cm cm}^{-2} \text{ s}^{-1} \text{ cmHg}^{-1}$), A is



effective membrane area (cm^2), L is the membrane skin layer thickness (cm), and ΔP is the transmembrane pressure difference (cmHg).

Permeability (P) is the product of solubility coefficient (S , cm^3 (STP) cmHg^{-1}) and diffusivity coefficient (D , $\text{cm}^2 \text{s}^{-1}$):

$$P = S \times D$$

For HFMs with ultrathin skin layers ($L < 1 \mu\text{m}$), permeance (P/L) is preferred and expressed in gas permeation units (GPU, $1 \text{ GPU} = 1 \times 10^{-6} \text{ cm}^3$ (STP) $\text{cm}^{-2} \text{s}^{-1} \text{cmHg}^{-1}$).^{32, 33} Solubility favors gases with high condensability and strong polymer-penetrant interactions (e.g., quadrupole interactions in polar polymers).³⁴ Diffusivity dominates in glassy polymers, where rigid chains create narrow free-volume distributions, preferentially passing smaller molecules.³⁵ Enhancing diffusivity requires smaller penetrant size, larger/more frequent free-volume elements, and increased polymer chain mobility.³⁴ The ideal selectivity of two gases is defined as follows:³⁶

$$\alpha_{A/B} = \frac{(P/L)_A}{(P/L)_B} = \left(\frac{S_A}{S_B}\right) \times \left(\frac{D_A}{D_B}\right)$$

where $(P/L)_A$ and $(P/L)_B$ denote the gas permeance of gases A and B, respectively, and S_A/S_B , D_A/D_B represent the solubility and diffusivity selectivity, respectively.

Polymeric HFMs exhibit an intrinsic permeability-selectivity trade-off.³⁷ Modifying polymers to enlarge free-volume elements often disproportionately benefits larger molecules (e.g., CH_4 over CO_2), decreasing selectivity.³⁸ This limitation arises from the inability to simultaneously increase free-volume size and narrow size distribution.³⁵ The empirical upper-bound relationship quantifies this trade-off:³⁵

$$P_i = k\alpha_{ij}^n$$

where P_i is permeability of the faster gas (Barrer), α is selectivity (P_i/P_j), and n is the slope dependent on gas-pair molecular diameters (d_i , d_j):³⁹

$$\frac{-1}{n} = \left(\frac{d_j}{d_i}\right)^2 - 1 = \left[\frac{d_j + d_i}{d_i^2}\right](d_j - d_i)$$

The coefficient k incorporates solubility and polymer free-volume distribution.⁴⁰



$$k^{-1/n} = \frac{S_i}{S_j} S_i^{-1/n} \exp \left\{ \frac{1}{n} \left[b - f \left(\frac{1-a}{RT} \right) \right] \right\}$$

where S_i and S_j are the solubility coefficients for gas i and j , $a = 0.64$ (universal constant), $b = 11.5$ (glassy polymers), and f is the polymer specific constant (52.633 kJ mol⁻¹ for 1991 upper bound and 59.234 kJ mol⁻¹ for 2008 upper bound).³¹

Molecular sieving in membrane-based gas separation operates through a well-defined activated diffusion mechanism that integrates two synergistic governing principles.⁴¹ First, steric exclusion effects arise from the precise size matching between gas molecules and membrane pore apertures, creating molecular-level filtration. Second, adsorption potential develops through specific interactions between gas molecules and pore walls, including van der Waals forces, electrostatic interactions, and surface chemistry effects.⁴¹ This dual-control mechanism establishes a distinct size-dependent transport behavior with three characteristic regimes. In the preferential transport regime, where gas molecules possess kinetic diameters substantially smaller than the pore dimensions, van der Waals interactions dominate, leading to enhanced surface adsorption and subsequent surface diffusion.⁴² The transition regime occurs when molecular dimensions approach the pore size, where steric repulsion creates substantial energy barriers that must be overcome by thermal activation.⁴² Finally, the exclusion regime emerges when molecular sizes exceed pore dimensions, resulting in near-complete rejection with selectivity factors exceeding 10³.⁴¹ These fundamental transport principles remain universally applicable across molecular sieve materials, with particular relevance to polymer-derived CMS hollow fiber membranes. Through pyrolysis at controlled temperatures, these membranes develop precisely tuned ultramicroporous networks that exhibit exceptional molecular discrimination. The pyrolysis process carefully balances carbonization and activation to optimize pore size distribution while maintaining structural integrity, enabling targeted separation of gas pairs such as CO₂/CH₄ and He/CH₄ with industrial-scale efficiency.

Surface diffusion achieves gas separation through two coupled processes:



selective adsorption of components with higher affinity onto pore surfaces, and surface migration via hopping between adsorption sites.⁴³ This mechanism dominates CO₂ separation in microporous membranes under low-temperature/high-pressure conditions, where enhanced adsorption selectivity drives performance.⁴³ Membranes leveraging surface diffusion contain slightly larger micropores than molecular sieves. The surface diffusion coefficient (D_s) follows Gilliland's model:⁴⁴

$$D_s = D_0^* e^{-\frac{E_a}{RT}}$$

$$E_a = a \cdot q$$

where D_0 is the pre-exponential factor, governed by adsorbed molecule vibration frequency and adsorption site spacing. E_a reflects the activation energy required for adsorbed molecules to jump between adjacent sites. a is a dimensionless scaling factor ($0 < a < 1$), relating to surface energy heterogeneity. q is the isosteric heat of adsorption representing adsorption strength. This formula reveals a critical trade-off: stronger adsorption (higher q) enhances selectivity but reduces mobility by increasing E_a , necessitating balanced q values in CO₂ separation membranes to avoid kinetic trapping.

The governing flow regime in porous membranes is determined by the Knudsen number ($Kn = \lambda/r$), where λ is the mean free path and r is the pore radius. Poiseuille flow dominates when $Kn \ll 1$ ($r > 10\lambda$), described by:⁴⁵

$$G = \frac{r^2}{8\mu} \frac{(p_f - p_p)}{L} \frac{p_{avg}}{RT}$$

$$p_{avg} = (p_f + p_p)/2$$

where p_f and p_p are the feed and permeate pressures, respectively, L is pore length, μ is gas viscosity, G is the viscous flow. Knudsen flow prevails when $Kn \gg 1$ ($r < 10\lambda$), where gas molecules collide primarily with pore walls rather than other molecules. Collisions scattered in random directions and the separation factors for gas molecules inversely proportional to the square root of molecular weight.⁴⁶ Both transport mechanisms provide inherently low selectivity due to insufficient molecular



discrimination.⁴⁵ Consequently, membranes operating predominantly under Knudsen or Poiseuille regimes are technologically unsuitable for high-performance gas separation application.

The solution-diffusion mechanism governs gas transport in dense polymeric layers, providing high selectivity while being fundamentally constrained by the permeability-selectivity trade-off. Molecular sieving (e.g., in carbon molecular sieves) enables precise size discrimination, although it requires sub-nanometer pore-size control (<0.7 nm) and exhibits vulnerability to aging-induced structural degradation. Surface diffusion enhances selectivity for condensable species (e.g., CO₂), but experiences diffusivity-selectivity compromises due to strong sorption hysteresis. Knudsen and Poiseuille flows yield separation factors below 5 ($\alpha < 5$), rendering them inadequate for molecular-level separations. Consequently, advanced membrane architectures integrate complementary mechanisms: ultrathin solution-diffusion skins enabling high-flux permeation, combined with molecular-sieving domains or surface-functionalized nanopores to achieve selectivity enhancement under aggressive industrial feed gas.

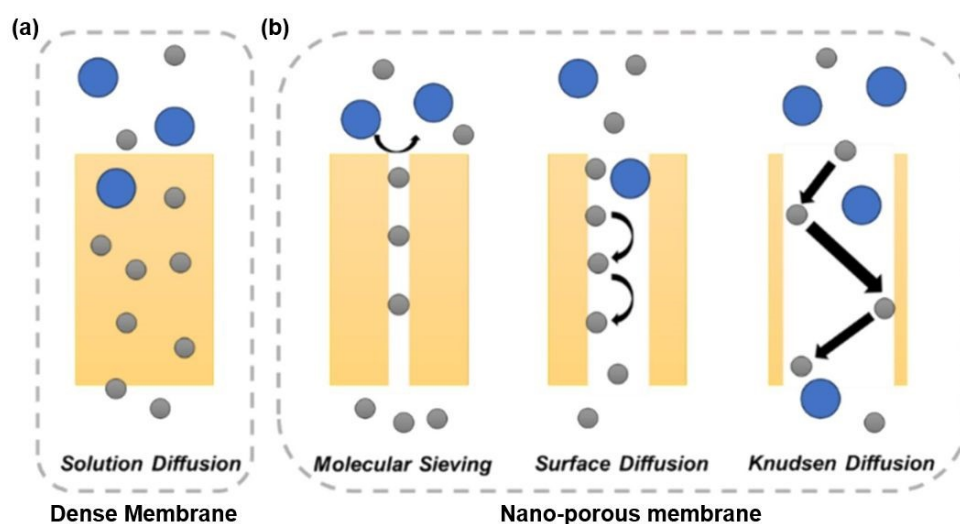


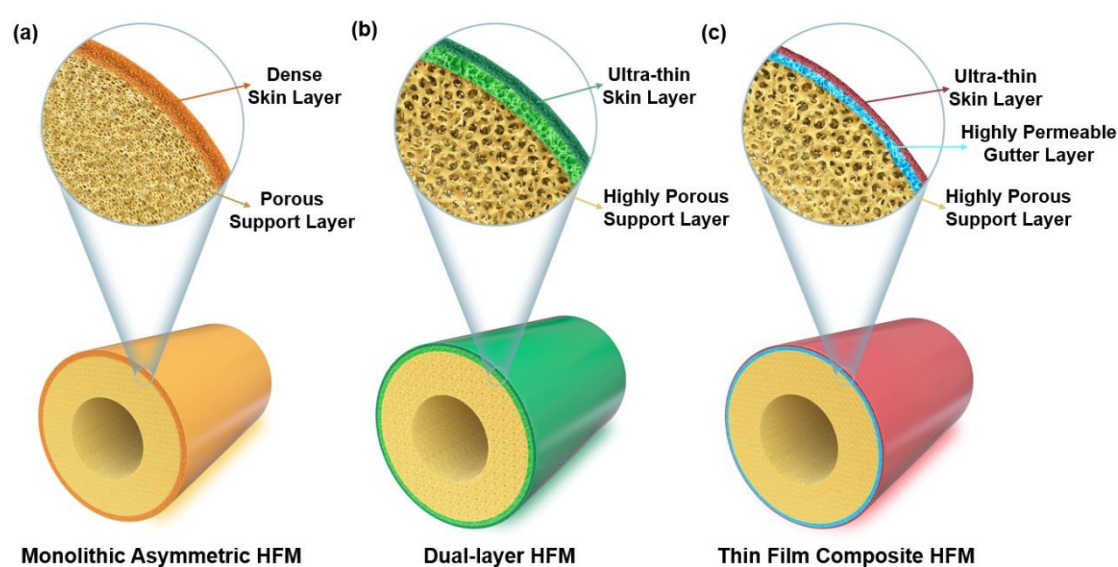
Fig. 3 Schematic for gas transport mechanisms of (a) solution-diffusion, (b) molecular sieving, surface diffusion, and Knudsen diffusion. Reproduced with permission from ref. 28 and Copyright 2024, Elsevier.

3 Configuration and fabrication of hollow fiber membranes

Building upon the gas transport fundamentals established in Section 2, where



258 solution-diffusion selectivity and interconnected free-volume elements govern
259 molecular separation, the architectural design of industrial hollow fiber membranes
260 strategically translates these principles into three performance-optimized
261 configurations. Asymmetric HFMs leverage ultrathin selective skins to maximize
262 permeance while minimizing resistance from the graded porous substructure (Fig. 4a).
263 Dual-layer HFMs intrinsically decouple structural functions: cost-effective supports
264 ensure mechanical robustness while high-performance selective layers determine
265 separation efficiency, with interfacial engineering providing synergistic integration to
266 prevent delamination (Fig. 4b).⁴⁷ TFC HFMs exploit nanoscale selective layers (<500
267 nm) deposited on optimized supports, enabling independent tuning of transport and
268 mechanical properties (Fig. 4c).⁴⁸ Collectively, these configurations demonstrate how
269 hierarchical structure-property relationships translate fundamental transport theory into
270 industrial performance.



272 **Fig. 4** Schematic of (a) monolithic asymmetric, (b) dual-layer, and (c) thin film
273 composite HFM.

274 3.1 Asymmetric outer selective layer HFM

275 The dry-jet/wet-quench spinning process remains the cornerstone for fabricating
276 asymmetric outer selective layer HFMs, offering unparalleled control over membrane
277 morphology and separation performance.⁴⁹ This process typically involves sequential



steps: (1) formulating polymer dope and bore fluids, (2) co-extrusion through a spinneret, (3) controlled phase separation in the air gap and coagulation bath, and (4) post-spinning treatment.⁵⁰ Critical performance determinants include dope formulation, processing parameters (e.g., air gap length, take-up speed), and post-treatment protocols, which collectively dictate the selective layer thickness, substructure porosity, and mechanical strength.⁵¹⁻⁵⁴ Dope optimization is guided by ternary phase diagrams (Fig. 5), where spinnable compositions lie near the binodal line in the one-phase region.⁵⁵ For instance, solutions with balanced polymer concentration (18-27%) and viscosity enable sufficient chain entanglement for fiber integrity while maintaining spinnability.⁵⁶ The solvent volatility ratio, controlled by blending low-volatility (e.g., N-methyl-2-pyrrolidone) and high-volatility solvents (e.g., tetrahydrofuran), precisely regulates solvent evaporation kinetics and phase inversion dynamics.^{53, 54} Increasing air gap length accelerates solvent evaporation, leading to the formation of denser and thicker skin layer.⁵⁴ Conversely, elevated coagulation bath temperatures accelerate solvent/non-solvent exchange rates, favoring porous substructures with lower mass transfer resistance.⁴⁹

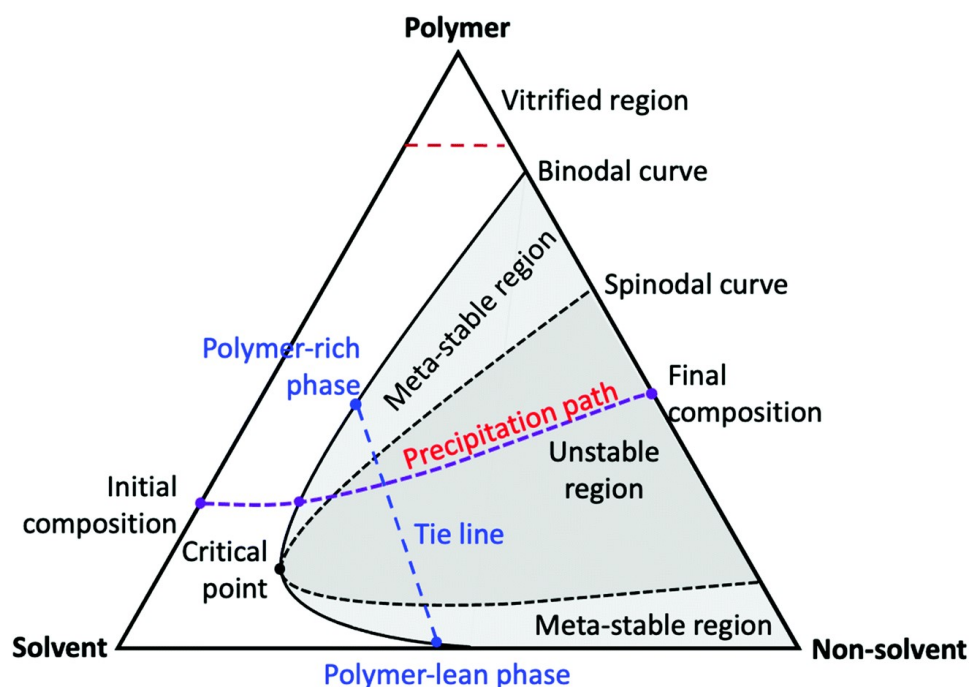


Fig. 5 Schematic ternary phase diagram of polymer-solvent-nonsolvent systems.



296 Reprinted with permission from ref. 23, copyright 2022, the Royal Society of Chemistry. View Article Online
DOI: 10.1039/D5TA04814A

297 Li et al.⁵⁷ developed defect-free 6FDA-mPDA_{0.9}-TFMB_{0.1} copolyimide HFMs for
298 He enrichment by optimizing polymer concentration and phase separation kinetics. At
299 <25 wt% polymer concentrations, porous substructures achieved He permeance of 72.1
300 GPU, while >30 wt% concentrations produced slightly thick skin layers (200-300 nm),
301 reducing permeance by 35%. By tuning air gap height (5 cm) and coagulation bath
302 composition (water/ethanol = 70:30), the resultant HFMs exhibited a burst pressure of
303 10.5 MPa and He/CH₄ selectivity of 178. Remarkably, these membranes retained
304 structural integrity under extreme conditions (750 PSIA mixed-gas feeds, -40 °C),
305 showing He permeance of 46 GPU and He/CH₄ selectivity of 429.⁵⁸ Similarly, Kosuri
306 et al.⁵⁹ engineered Torlon® HFM for high-pressure CO₂ separation by suppressing
307 macrovoids through increased polymer concentration (28 wt%) and elevated dope
308 temperatures (60 °C). The optimized membranes achieved CO₂/CH₄ selectivity of 39.6
309 under 1100 PSIA feed pressure at 35 °C, demonstrating suitability for industrial high-
310 pressure natural gas upgrading.

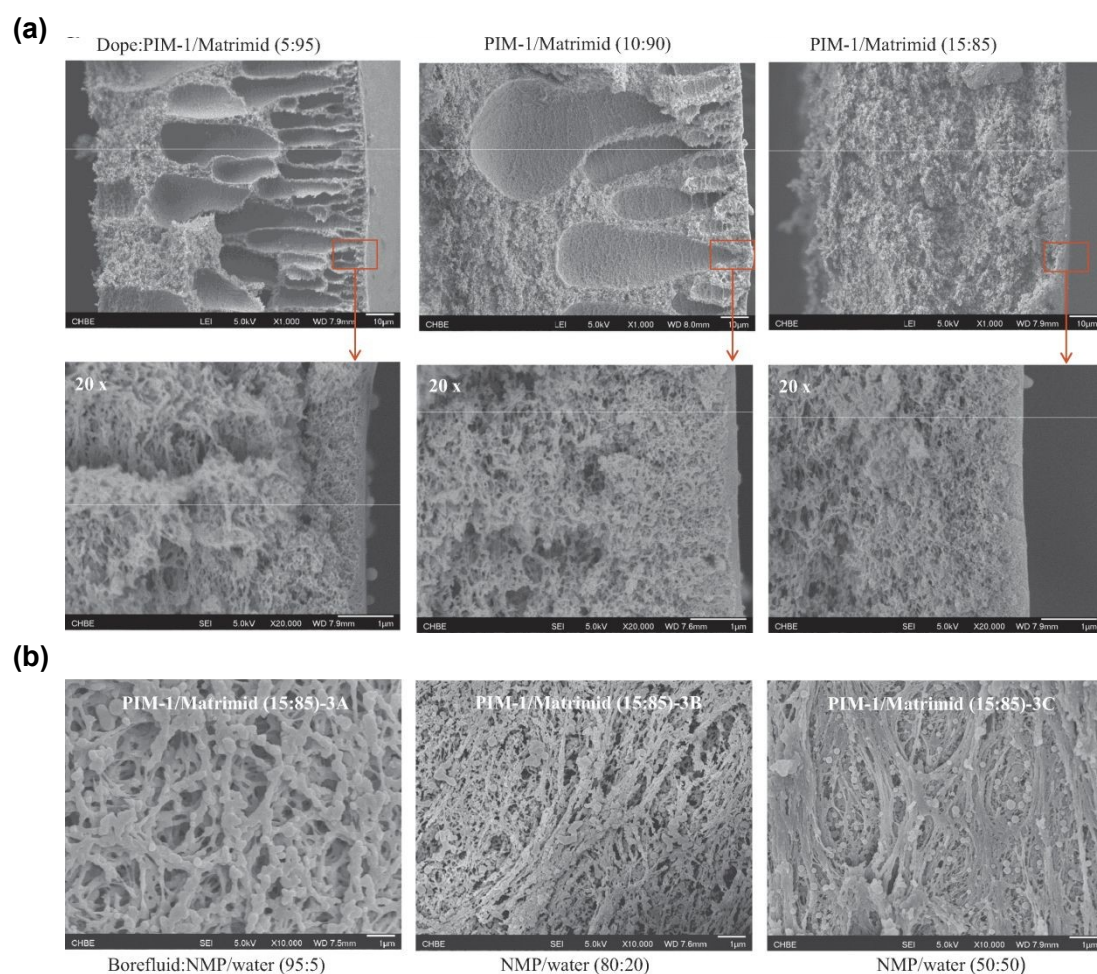
311 Polymer blending offers a cost-efficient approach to enhance hollow fiber
312 membrane (HFM) performance by combining complementary properties of base
313 polymers and additives. Yong et al.⁶⁰ demonstrated this strategy by incorporating 5-15
314 wt% PIM-1 into Matrimid® dopes, achieving ultrathin selective layers (30-70 nm) (Fig.
315 6a). The blend HFMs exhibited CO₂ permeance increases of 78% (153.4 GPU) and 146%
316 (212.4 GPU) at 5 wt% and 10 wt% PIM-1 loadings, respectively, while maintaining
317 CO₂/CH₄ selectivity >26. Further optimization with 15 wt% PIM-1, 95:5 NMP:H₂O
318 bore fluid, and silicone rubber coating improved CO₂ permeance to 243.2 GPU and
319 CO₂/CH₄ selectivity of 34 by sealing surface defects (Fig. 6b-c). However, PIM-1's
320 limited solubility constrained blending ratio. To address this critical limitation, Jue et
321 al.⁶¹ developed a triple-orifice spinneret for coextruding PIM-1 dope with a protective
322 sheath layer of 1-butanol/THF (Fig. 6d). This approach reduced volatile solvent THF
323 evaporation relative to polymer dope directly exposed to air, yielding defect-free



Open Access Article. Published on 14 August 2025. Downloaded on 8/19/2025 5:34:33 AM.
This article is licensed under a Creative Commons Attribution-NonCommercial 3.0 Unported Licence.


Journal of Materials Chemistry A Accepted Manuscript

324 asymmetric HFMs with a 3-6 μm skin layer. These HFMs initially achieved CO_2
325 permeance of 540 GPU and selectivity of 25, stabilizing at 360 GPU and CO_2/CH_4
326 selectivity of 23 after two-month aging. In a complementary additive approach, Hu et
327 al.⁶² incorporated 0-12 wt% polyethylene glycol (PEG) as a CO_2 -philic additive into
328 dope solution for Matrimid[®] 5218 HF spinning. Increasing PEG concentration
329 accelerated phase separation during membrane formation, producing hollow fibers with
330 higher porosity and thinner selective skin and elevating CO_2 permeance from 21 GPU
331 (neat Matrimid[®]) to 37 GPU (12 wt% PEG).



332

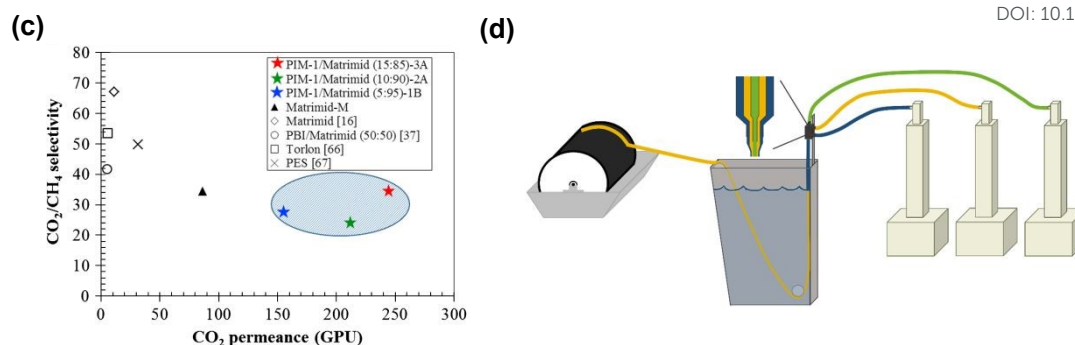


Fig. 6 (a) Selective layer thickness versus PIM-1 content in PIM-1/Matrimid® blend HFMs. (b) Inner surface morphology of PIM-1/Matrimid® (15:85 ratio) fibers fabricated with different bore fluids. (c) CO₂/CH₄ separation performance of PIM-1/Matrimid blends HFMs. Reprinted with permission from ref. 59, copyright 2013, Elsevier. (d) Spinning apparatus employing a triple-orifice spinneret for simultaneous coextrusion of sheath fluid (blue), polymer dope (yellow), and bore fluid (green). Reprinted with permission from ref. 60, copyright 2017, Elsevier.

3.2 Dual-layer hollow fiber membrane

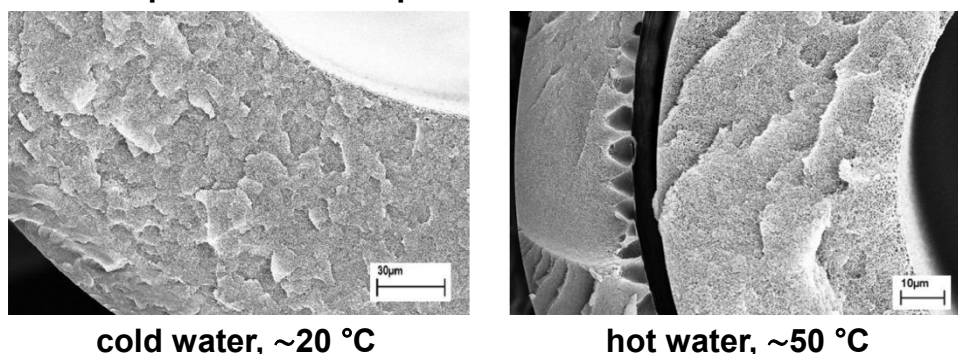
Dual-layer hollow fiber membranes (DLHFMs), integrating a high-performance, expensive, thin selective outer layer and a cheap, porous support layer, have emerged as a cost-effective strategy for gas separation by minimizing the use of high-performance polymers.⁶³ Fabrication primarily via co-extrusion spinning, DLHFMs require precise control over dope rheology of the two distinct polymer solutions, air gap distance, and coagulation bath composition to ensure interfacial adhesion and structural integrity.⁶⁴ Key challenges include delamination from mismatched shrinkage rates and defective interfaces caused by shear stress variations during co-extrusion.⁶⁵ Jiang et al.⁶⁶ demonstrated that increasing inner dope polymer concentration (polysulfone: 25% to 30%) reduced shrinkage during phase inversion, enabling robust adhesion of the outer Matrimid® layer. Optimized conditions yielded DLHFMs with CO₂ permeance of 11 GPU and CO₂/CH₄ selectivity of 40. Raza et al.⁶⁷ further revealed a V-shaped CO₂ permeance-air gap relationship (minimum at 5 cm) and Λ-shape CO₂/CH₄ selectivity profile (peak at 5 cm) for cellulose triacetate (CTA)-cellulose diacetate (CDA)/CTA dual-layer HFMs, achieving 45 GPU CO₂ permeance and 30.3 CO₂/CH₄ selectivity at 1 mL min⁻¹ outer dope flow rate with a take-up speed of 15 m



min⁻¹, double the permeance without sacrificing selectivity compared to single-layer counterparts.

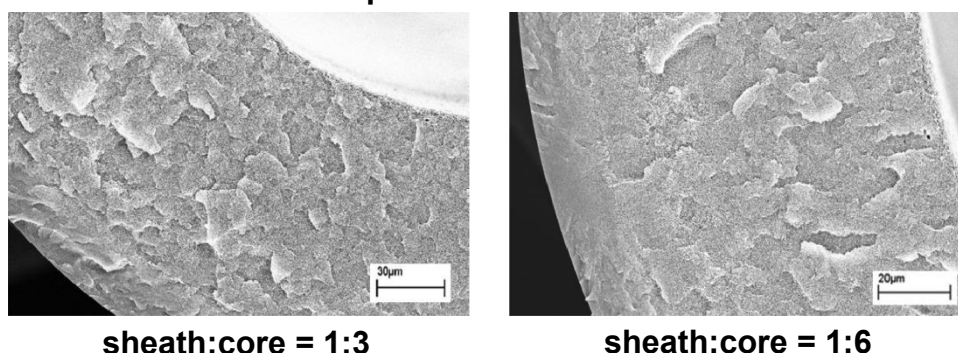
Surface modification and crosslinking strategies significantly enhance separation performance of DLHFMs. Li et al.⁶⁸ fabricated DLHFMs using coextrusion technology where both inner and outer layers consisted of polyethersulfone (PES) with different polymer concentrations of 23 wt% and 35 wt%, respectively. These HFMs subsequently underwent surface modification through a three-step chemical treatment: chloromethylation, sulfonation, and silver ion exchange. The incorporated silver ions selectively enhanced CO₂ transport via quadrupole interactions, achieving exceptional CO₂/CH₄ selectivity of 118 with CO₂ permeance of 25.1 GPU. Liu et al.⁶⁹ chemically crosslinked the outer 6FDA-durene-mPDA layer of the 6FDA-durene-mPDA/PES DLHFMs with *p*-xylylenediamine, forming rigid networks that boosted CO₂/CH₄ selectivity to 101 despite reduced CO₂ permeance (28.3 GPU). Ma et al.⁷⁰ engineered ester-cross-linkable Torlon®/6FDA-DAM:DABA (3:2) DLHFMs, where optimized quench bath temperature (50 °C), sheath/core flow ratios (1:3), and air gap residence time of 0.04 s yielded defect-free fibers (Fig. 7a-c). Crosslinked hollow fibers demonstrated stable CO₂ permeance (40 GPU) and CO₂/CH₄ selectivity (39) under 100 PSIA feeds (CO₂/CH₄, 50/50 v/v) containing 1000 ppm toluene, highlighting industrial viability.



(a) Different quench bath temperatures

cold water, ~20 °C

hot water, ~50 °C

(b) different sheath/core dope flow rate ratios

sheath:core = 1:3

sheath:core = 1:6

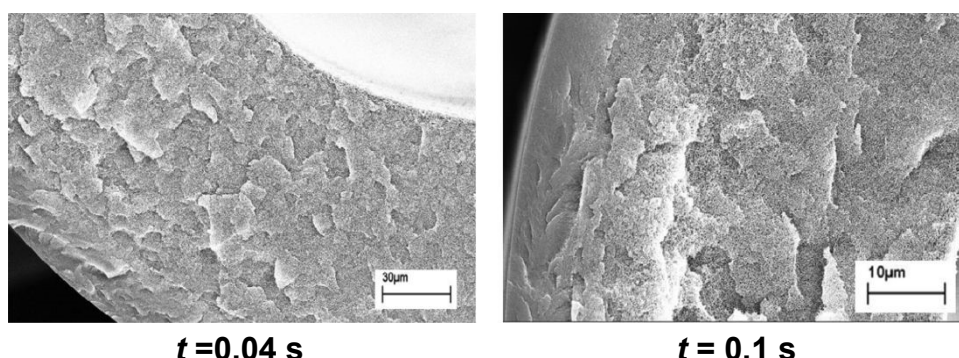
(c) different air gap residence time $t = 0.04 \text{ s}$ $t = 0.1 \text{ s}$

Fig. 7 SEM images of PDMC/Torlon[®] composite hollow fibers under varied processing conditions: (a) quench bath temperature, (b) sheath/core flow ratio, and (c) air gap residence time. Reprinted with permission from ref. 69, copyright 2013, American Chemical Society.

Filler incorporation in DLHFM enhances performance through complementary mechanisms: molecular sieving via filler nanopores improved gas affinity through functional groups (e.g., amine-CO₂ interactions), and tuned polymer chain packing that suppresses non-selective pathways. However, filler loading exceeding 5 wt% can create interfacial defects, necessitating surface modifications for uniform dispersion.⁷¹ For



instance, Khan et al.⁷² incorporated polyethyleneimine (PEI)-functionalized bimetallic MOF (PEI@HKUST-1(Cu, Mg)) exclusively into the outer layer dope with polysulfone (PSf) utilized as polymer in both inner and outer dope for DLHFM spinning. The amine groups from PEI-MOFs enhanced CO₂ affinity while open metal sites combined with high porosity provided additional CO₂ binding sites and transport channels. The synergistic design promoted rapid CO₂ permeation, yielding 75% higher CO₂ permeance (28 GPU) and 85% improved CO₂/CH₄ selectivity (51) compared to unmodified PSf HFMs.

3.3 Thin film composite HFMs

Thin-film composite (TFC) HFMs overcome limitations of monolithic designs through a decoupled fabrication strategy. First, a porous polymeric support (e.g., polysulfone, polyimide) is formed via phase inversion. Subsequently, an ultrathin selective layer (under 1 μm thickness) is deposited via dip coating or interfacial polymerization.⁷³⁻⁷⁶ This sequential approach enables independent optimization of support morphology (pore size, porosity, surface chemistry) and selective layer properties (thickness, crosslink density, functionality), achieving unprecedented permeance-selectivity combinations.^{77, 78} Dip coating-recognized as the most industrially viable technique-involves immersing HFM substrates into coating solutions. Final membrane performance critically depends on substrate properties, pre-wetting protocols and process parameters including solution concentration, withdrawal speed, and curing conditions.⁷⁹⁻⁸¹ Qin et al.⁸² fabricated polysulfone (PSf)/poly (4-vinylpyridine) (4-PVP)/silicon rubber (SR) multilayer composite membranes via dip-coating. They controlled PSf substrate's pore size by adjusting diethylene glycol (DEG) content (nonsolvent additive) during phase inversion. Pre-wetting proved essential for preventing coating penetration into large-pore substrates. Using optimized DEG content with 5 wt% and pre-wetting, they achieved CO₂ permeance of 92 GPU and CO₂/CH₄ selectivity of 29 at 25 °C and 200 psi. Li et al.⁸³ optimized polyvinylamine/polyvinyl alcohol (PVAm/PVA) coatings on PSf HFMs using



orthogonal experimental design. Key parameters including 20 wt% PSf concentration and PEG-400 additive. The resulting composite HFMs with selective layer thickness of 160-nm delivered CO₂ permeance of 52 GPU with CO₂/CH₄ selectivity of 24 under mixed-gas conditions (CO₂/CH₄, 40/ 60, v/v), outperforming conventional cellulose acetate HFM.

Material innovations in TFC HFMs now strategically address two critical industry barriers: reducing the environmental footprint of membrane manufacturing and overcoming permeance-selectivity trade-offs. Theodorakopoulos et al.⁸⁴ demonstrated these by engineering P84 co-polyimide/Pebax-1657 composite HFMs. They replacing toxic N-methyl-2-pyrrolidone (NMP) with greener γ -butyrolactone (GBL) in support HFs fabrication, reducing solvent toxicity while maintaining spinnability. Simultaneously, graphene nanoplatelets (GNPs) incorporated in both support and selective layers enhanced separation performance. The resulting (G_{Green}/Pebax+GNPs)/P84 composite HFMs achieved CO₂/CH₄ selectivity of 82 and He/N₂ selectivity of 20, with CO₂ and He permeances of 3GPU and 2.7GPU respectively under binary gas testing (1.3 bar, 25 °C). Complementing solvent and nanofiller innovations, novel polymer architecture also could enhance TFC HFM separation performance. Gutierrez-Hernandez et al.⁸⁵ coated PIM-1 with 11% side-chain substitution as selective layer on PP-HF impregnated PDMS. The B-PIM-1/PDMS/PP HFMs achieved CO₂ permeance of 650 GPU and CO₂/CH₄ selectivity of 14.

Interfacial polymerization (IP) enables ultra-thin (<500 nm), chemically tailored selective layers through controlled monomer diffusion.^{59, 86} Jo et al.⁸⁷ polymerized trimesoyl chloride (TMC) and 1,3-cyclohexanebis-methylamine (CHMA) on PSf HFMs, where CHMA concentration governed crosslinking density. At 1.0% CHMA/0.5% TMC, the membrane achieved CO₂ permeance of 25 GPU and CO₂/CH₄ selectivity of 28. Choi et al.⁸⁸ fabricated He-selective membrane via m-phenylenediamine (m-PDA)/TMC IP on PAN supports, followed by PTMSP gutter



layer deposition. The resultant membrane exhibited He permeance of 46.2 GPU and He/CH₄ selectivity of 11.9. Future directions integrate machine learning (ML) to optimize curing kinetics and monomer ratios. Neural networks trained on experimental datasets could predict optimal dip-coating parameters for target selectivity.^{89, 90} ML models can bridge molecular design with process engineering, accelerating the development of TFC HFMs for extreme industrial conditions (e.g., high-pressure natural gas feeds).

3.4 Complementary strategies and synergistic innovations

The asymmetric, dual-layer, and thin-film composite hollow fiber membranes establish complementary roles in natural gas valorization through distinct economic and operational advantages. Dual-layer configurations strategically combine high-performance selective polymers such as 6FDA polyimides with economical supports like polysulfone, reducing material costs by 40–60% while preserving over 90% separation efficiency. This design excels in cost-sensitive applications including marginal natural gas fields. Asymmetric membranes deliver superior stability under aggressive conditions, where crosslinked variants withstand CO₂ partial pressures exceeding 500 PSIA, making them indispensable for bulk acid gas removal. Thin-film composites enable module-level retrofitting, where advanced coatings (e.g., PIM-1 derivatives) achieve permeance enhancement without infrastructure modification, enabling economical helium recovery from sub-0.3% sources.

Emerging synergies bridge different membrane architectural paradigms through cross-technology integration. Electrospinning also offers significant potential for fabricating HFMs with tunable nanofibrous architectures and enhanced surface functionalities, enabling novel transport pathways for gas separation. Recent advances in coaxial spinning techniques demonstrate promising routes toward scalable hollow fiber production, complementing conventional fabrication methods.⁹¹ Hybrid fabrication enables co-extruded dual-layer supports to host ultrathin selective skins via interfacial polymerization, eliminating delamination while enhancing molecular



sieving. Concurrently, machine learning-guided architecture selection dynamically matches membrane types to feed conditions: thin-film composites HFM for CO₂-dominant streams and asymmetric HFMs for helium enrichment scenarios. These fabrication innovations directly enable the advanced polymers discussed in Section 4, where hierarchical structures (e.g., DLHFMs) maximize the performance of emerging materials like TR polymers and CMS. Collectively, these pathways advance hollow fiber membranes toward adaptive, economically viable gas separation systems that maintain industrial robustness while addressing evolving sustainability imperatives.

4 Select relevant polymers for HFM

Polymeric materials underlie the vast majority of hollow fiber membrane configurations, with fabrication processes requiring balanced solution processability, mechanical robustness, and gas separation performance. Key commercially established materials include cellulose acetate (CA), polysulfone (PS), polyimide (PI), alongside emerging candidates like thermally rearranged (TR) polymers and carbon molecular sieves (CMS) (Fig. 8). These polymers exhibit critical structural attributes: (1) chain rigidity (e.g., aromatic rings in PI, fused bicyclic units in PIMs) that enhances size-sieving selectivity via restricting polymer chain mobility; (2) asymmetric/contorted backbones (e.g., spirobisindane in PIM-1) that create interconnected free-volume elements for fast gas transport; (3) functional groups (e.g., sulfone groups in PS, imide rings in PI) that confer chemical stability under harsh conditions; and (4) solvent compatibility, enabling dissolution and phase inversion into defect-free hollow fibers.⁹²⁻⁹⁴ This section systematically evaluates relevant HFM materials by elucidating their intrinsic transport properties, analyzing advanced modification strategies, and identifying key challenges for sustainable manufacturing.



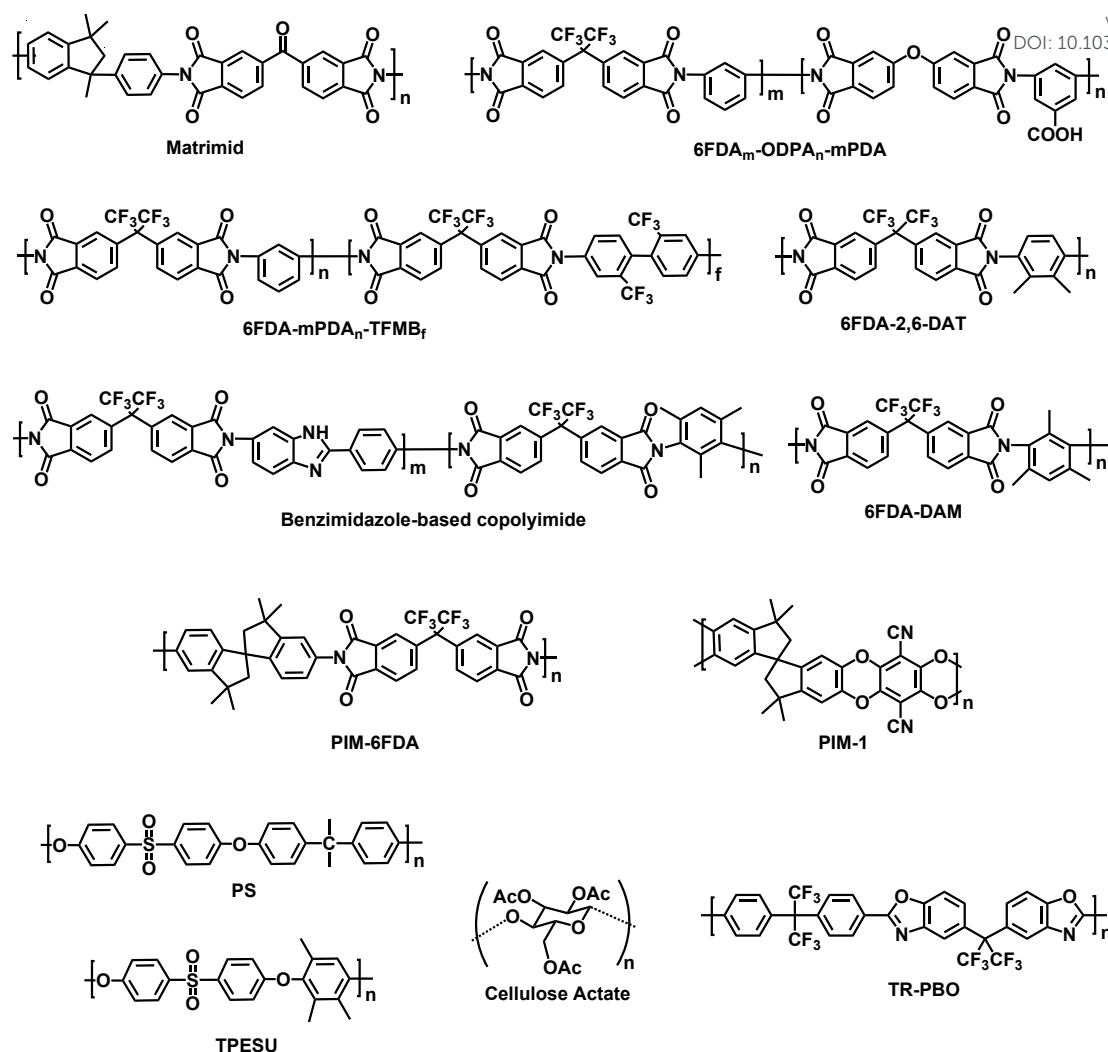


Fig. 8 Representative chemical structures of HFM polymers.

4.1 Cellulose acetate (CA)

Cellulose acetate (CA), derived from renewable cellulose via acetylation, has been a cornerstone material for gas separation membranes since the 1980s due to its low cost, tunable hydrophilicity, and inherent CO₂ affinity.⁹⁵⁻⁹⁷ The degree of substitution (DS = 2.4-2.8) critically governs membrane performance: cellulose triacetate (CTA) exhibits higher free volume compared to partially acetylated CA, enhancing CO₂ permeance of 10-15 GPU but increasing susceptibility to CO₂-induced plasticization.^{98, 99} Bulky acetyl groups disrupt cellulose's crystalline structure, creating amorphous regions that facilitate gas diffusion while maintaining mechanical stability.¹⁰⁰ Recent advances focus on optimizing spinning parameters and post-treatments to enhance the gas separation performance of CA-based HFM.^{101, 102} Pak et al.¹⁰³ demonstrated that



reducing tetrahydrofuran/ethanol (THF/EtOH) ratio in spin dopes from 3:1 to 1:1 slowed precipitation rate, forming denser skin layers with 30% fewer defects. Coupled with a 15 cm air gap for enhancing molecular orientation, PDMS-coated CA HFMs achieved CO₂ permeance of 12.9 GPU and CO₂/CH₄ selectivity of 43.8 at 3 bar, surpassing unmodified membranes by 70% in selectivity. Mubashir et al.¹⁰⁴ revealed a V-shaped permeance-air gap relationship and Λ -shaped selectivity profile for CA HFMs, with optimized take-up speeds yielding CO₂/CH₄ selectivity of 7.9. PDMS coating outperformed thermal annealing (120 °C) by sealing macrovoids, improving CO₂/CH₄ selectivity by 70.9%.

Incorporating nanoparticles into cellulose acetate matrices produces mixed matrix hollow fiber membranes (MMHFMs) with enhanced CO₂/CH₄ separation performance. Strategic manipulation of spinning parameters minimizes interfacial voids in these MMHFMs, further improving their gas separation efficiency. For instance, Mubashir et al.¹⁰⁵ fabricated NH₂-MIL-53(Al)/CA MMHFMs containing 15 wt% MOF by optimizing take-up speed and air-gap distance. They observed that increasing take-up speed improved ideal selectivity by 40% due to shear-induced molecular alignment, while air-gap variations produced distinct “V” and “ Λ ” patterns. At optimal conditions (12.2 m min⁻¹ take-up speed, 5.0 cm air gap), the membrane achieved a CO₂/CH₄ ideal selectivity of 16.0 with CO₂ permeance of 6.7 GPU at 25 °C and 3 bar feed pressure. In a follow-up study using design of experiments, they demonstrate that increasing permeance testing temperature from 30 °C to 50 °C reduced the CO₂/CH₄ separation factor of MMHFMs due to accelerated polymer chain relaxation, whereas elevating feed pressure from 3 to 15 bar and CO₂ feed composition from 15 to 42.5 vol% enhanced separation performance. Feed pressure emerged as the dominant factor, reducing CH₄ permeance by 32% while marginally lowering CO₂ permeance, yielding a maximum CO₂/CH₄ separation factor of 14.4 at 15 bar, 30 °C, and 15 vol% CO₂.¹⁰⁶ Similarly, Sunder et al.¹⁰² fabricated NH₂-MIL-125(Ti)/CTA MMHFMs via a 1 cm air-gap process, where dual PDMS coating reduced surface defects but introduced



permeance loss (35%) due to thicker coating. The modified membranes exhibited CO_2/CH_4 ideal selectivity of 6.87 and CO_2 permeance of 26.46 GPU.

4.2 Polysulfone (PS)

Polysulfone (PS), with its alternating sulfone ($-\text{SO}_2-$) and biphenyl groups, serves as an industry-standard polymer for gas separation membranes due to exceptional thermal stability, chemical resistance, and mechanical robustness under high-pressure conditions.¹⁰⁷ The electron-withdrawing sulfone groups promote dense chain packing, resulting in a low fractional free volume of approximately 5%. Consequently, while CO_2 permeance remains 20-30 GPU, size-sieving selectivity for small molecules is enhanced.¹⁰⁸⁻¹¹⁰ Commercial PS variants, synthesized via nucleophilic substitution between 4,4'-dichlorodiphenylsulfone (DCDPS) and bisphenols, achieve tunable properties through backbone modifications.¹¹¹ For instance, Yong et al.¹¹² synthesized poly(trimethyl phenylene ether sulfone) (PESU) by replacing one diphenyl sulfone unit with a bulky and rigid 1,2,4-trimethylbenzene moiety, which introduced additional free volume and suppressed chain relaxation. The resultant HFMs exhibited CO_2 permeance of 85.1 GPU and CO_2/CH_4 selectivity of 35.5 at 3.5 bar, with aging rates reduced by 60% compared to conventional PS.

The gas separation performance of PS HFMs is highly sensitive to spinning parameters and post-treatment conditions. Lower dope solution temperatures (T_d) and coagulation bath temperatures (T_c) slow solvent-non-solvent exchange rates, promoting denser skin layers with reduced macrovoids formation.⁶⁶ Liu et al.¹¹³ demonstrated that reducing T_d from 35 °C to 3 °C and T_c from 25 °C to 7 °C minimized finger-like macrovoids, yielding membranes with CO_2 permeance of 53.5 GPU. However, unmodified PS HFMs exhibit low selectivity ($\text{CO}_2/\text{CH}_4 \approx 1.24$), necessitating post-coating treatments. Silicone rubber (PDMS) coating (3 wt%) on optimized PS HFMs enhanced selectivity to 39.4 while maintaining CO_2 permeance at 31.9 GPU. Roslan¹¹⁴ et al. further showed that increasing polysulfone polymer concentration (from 15 to 35 wt%) in spin dopes reduced gas permeance by 45% but improved CO_2/CH_4 selectivity by 150%



due to denser membrane structures. Multilayer coating (3 wt% PDMS + 3 wt% Pebax®-1657) on PS HFM achieved optimal performance (CO₂ permeance of 21.12 GPU and CO₂/CH₄ selectivity of 34.28), outperforming single-layer PDMS by 87% in permeance.

PS serves as an ideal matrix for mixed-matrix and thin-film composite HFMs. Khan et al.¹¹⁵ incorporated 0.5 wt% ZIF-8 into PSf HFMs, leveraging molecular sieving and CO₂-philic open metal sites to achieve CO₂ permeance of 47.75 GPU and CO₂/CH₄ selectivity to 25.7. Sasikumar et al.¹¹⁶ engineered amine-modified SiO₂ and ZIF-8 MM-HFMs with Pebax®-1657 coating, where amine groups enhanced CO₂ affinity, yielding CO₂ permeance of 41.15 GPU and CO₂/CH₄ selectivity of 22.25. Sharif et al.¹¹⁷ developed PES-based nanocomposite HFMs with PVP/PDMS/SiO₂ skin layers, achieving CO₂/CH₄ selectivity of 45, CO₂ permeance of 102 GPU, and tensile strength of 58 MPa, a 40% improvement over pristine PS.

4.3 Polyimide (PI)

Aromatic polyimides (PIs), synthesized via polycondensation of aromatic dianhydrides and diamines, are distinguished by their highly tunable gas separation properties and exceptional thermal/mechanical stability, positioning them as premier materials for natural gas purification.^{118, 119} Successful fabrication of polyimide HFMs critically hinges on precise control over polymer architecture, molecular weight distribution, and purity during dope preparation, in which only small variations in the polymer structure can significantly impact the ability to form a workable dope.⁵⁵ Random copolymers with minimal block/branch structures prevent localized aggregation and maintain homogeneous solution rheology for stable fiber spinning. Conversely, block or branched architectures promote gelation due to enhanced intermolecular associations and topological entanglements in solution, driven by microphase separation tendencies of chemically distinct segments. Optimal molecular weight balances chain entanglement for fiber integrity against excessive viscosity, while residual monomers and cyclic oligomers must be eliminated to avoid phase separation during spinning. These material parameters collectively govern solvent-



polyimide interactions.

Soluble homopolyimides, such as 6FDA/DAM and Matrimid[®], are commonly used due to their ability to form workable dope.⁵⁵ The rigid backbone architecture, characterized by kinked structures (e.g., the phenylindane moiety in Matrimid[®]) and bulky substituents (e.g., hexafluoroisopropylidene groups in 6FDA), generates a tunable free-volume fraction (15-25%) that directly governs gas transport.^{92, 120, 121} For instance, Matrimid[®] 5218 (BTDA-DAPI) achieves CO₂ permeance of 17.7 GPU and CO₂/CH₄ selectivity of 24.3 at 2 bar, surpassing polyethersulfone HFM by 50% in CO₂/CH₄ selectivity under comparable conditions.^{121, 122} Cao et al.¹²³ developed 6FDA-2,6-DAT HFMs via NMP-based spinning, showing initial CO₂ permeance of 300 GPU. Physical aging reduced permeance to 76 GPU over 185 days due to free-volume collapse, but mixed-gas tests (CO₂/CH₄ = 50/50) showing stabilized permeance at 59 GPU with CO₂/CH₄ selectivity of 40, highlighting industrial viability. Gutierrez-Hernandez et al.¹²⁴ fabricated 6FDA-TMPD TFC HFMs using polypropylene hollow fibers as porous supports and highly permeable PDMS as blocking layer to mitigate the intrusion of 6FDA-TMPD. The membrane achieved CO₂ permeance of 54.5 GPU and CO₂/CH₄ selectivity of 13.9 under CO₂/CH₄ (50:50 vol%) gas mixtures, demonstrating stable performance up to 30 bar.

Spinning parameters optimization (e.g., dope solvent selection, polyimide concentration) critically impacts polyimide HFM microstructure and gas separation performance. Hachisuka et al.¹²⁵ demonstrated that diethylene glycol dimethyl ether (DGDE) as the good solvent produces defect-free 6FDA-BAAF HFMs with ultrathin selective layer, achieving CO₂ permeance of 550 GPU and CO₂/CH₄ selectivity of 27. In contrast, NMP generates finger-like macrovoids due to rapid phase separation, reducing selectivity by 35%. Qin et al.¹²⁶ optimized shear rates during 6FDA-Durene/mPDA fiber spinning, yielding defect-free structures with CO₂ permeance of 53.3 GPU and CO₂/CH₄ selectivity of 42.9 after post-PDMS coating, outperforming dense films by 29% in selectivity. Besides, lower molecular weight PIs require



adjusting dope formations to maintain spinnability. Xu et al.¹²⁷ increased polymer concentration and reduced ethanol/LiNO₃ additives to suppress phase separation, achieving defect-free HFMs with CO₂/CH₄ selectivity of 22.7 (29% higher than dense films). This highlights the inverse relationship between molecular weight and required polymer concentration for optimal fiber formation.

4.4 Thermally rearranged polymer

Thermally rearranged (TR) polymers-typically derived from ortho-functionalized polyimide precursors (e.g., hydroxyl-containing polyimides) via controlled pyrolysis (400-450 °C),^{128, 129} forming rigid heterocyclic structures (e.g., polybenzoxazoles, PBO) with ultra-high fractional free volume.^{130, 131} Their bimodal pore architecture combines ultramicropores (<7 Å) for precise molecular sieving with interconnected micropores (>10 Å) for rapid gas transport, positioning them ideally for CO₂/CH₄ separation.¹³² However, substructure collapse during pyrolysis thickens selective layers and reduces permeance by up to 40% versus precursors.¹³³ Recent advances mitigate this through precursor engineering and crosslinking strategies.

Kim et al.¹³⁴ minimized substructure collapse by first conducting thermal imidization at 300 °C on hydroxyl poly(amic acid) precursors, stabilizing the fiber morphology, before thermal rearrangement at 450 °C for 60 min. The resulting TR-PBO HFMs achieved CO₂ permeance of 1938 GPU and CO₂/CH₄ selectivity of 14 with a 2 µm selective layer-retaining 60% higher permeance than conventional TR-HFMs. To enhance selectivity while preserving permeance, Fan et al.¹³⁵ designed phenolphthalein-modified 6FDA-DAP:DAM (1:2) precursors. Sub-Tg crosslinking (via lactone ring opening) locked the polymer network, preventing pore coalescence during pyrolysis. Subsequent thermal rearrangement at 400 °C generated slit-like ultramicropores, yielding CO₂ permeance of 436.22 GPU and CO₂/CH₄ selectivity of 30.63, a 120% selectivity jump over non-crosslinked TR analogs without permeance sacrifice. These collective advances demonstrate that TR polymer performance hinges critically on preserving pore architecture integrity during rearrangement, a challenge

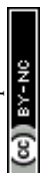


now addressable via molecular-scale precursor control.

4.5 Carbon molecular sieves

Carbon molecular sieve (CMS) HFMs achieve exceptional gas separation performance through their hierarchical pore architecture, where micropores (7-20 Å) facilitate rapid transport while ultramicropores (<7 Å) function as molecular sieves.^{136, 137} Pore structure modulation strategies include precursor design, pyrolysis conditions optimization, and post-synthesis modifications.¹³⁸⁻¹⁴¹ Vu et al.¹⁴² demonstrated that vacuum pyrolysis of 6FDA/BPDA-DAM at 550 °C yielded CMS membranes with CO₂ permeance of 25-30 GPU and CO₂/CH₄ selectivity of 73-85, outperforming Matrimid®-derived CMS with CO₂ permeance of 11-13 GPU and CO₂/CH₄ selectivity of 69-83. Precise pyrolysis temperature control adjusts ultramicroporous gateways for target molecules. Zhang et al.¹⁴³ demonstrated that pyrolysis >875 °C refines ultramicropores to 4.0-4.5 Å (Fig. 9a-b), creating “selective adsorption sites” within a less selective carbon matrix. The carbon/carbon mixed-matrix (CCMM) membranes pyrolyzed at 900 °C demonstrated unprecedented separation performance, achieving CO₂/CH₄ selectivity of 3650 and He/CH₄ selectivity of 16,700. This exceptional performance results from the synergistic combination of size exclusion and adsorption affinity, which surpasses the diffusion-limited selectivity of traditional CMS materials. Structural characterization by WAXRD and Raman spectroscopy (Fig. 9c-d) confirms that the CMS samples consist of highly disordered amorphous domains.

Precursor-derived chemistry and post-synthesis functionalization fine-tunes microporosity and gas separation performance of HFMs. Kamath et al.¹⁴⁴ retained 18.5% fluorine (-CF₃ groups) in 6FDA-DETDA:DABE CMS HFMs via a two-stage pyrolysis protocol: crosslinking at 370 °C followed by carbonization at 500 °C under argon, which expanded free volume while narrowing pore size distribution. The resultant membranes exhibited CO₂ permeance of 552 ± 28 GPU, with CO₂/CH₄ selectivity of 37.0 ± 4. Wu et al.¹⁴⁵ fluorinated partially carbonized 6FDA_{0.9}-ODPA_{0.1}-mPDA HFMs, polarizing pore wall through C-F bonds. This strengthened H₂ interaction and reduced



effective pore size, boosting He/H₂ selectivity from 3.1 to 9.7, while maintaining He permeance >100 GPU ($\alpha(\text{He}/\text{CH}_4) = 2193$).

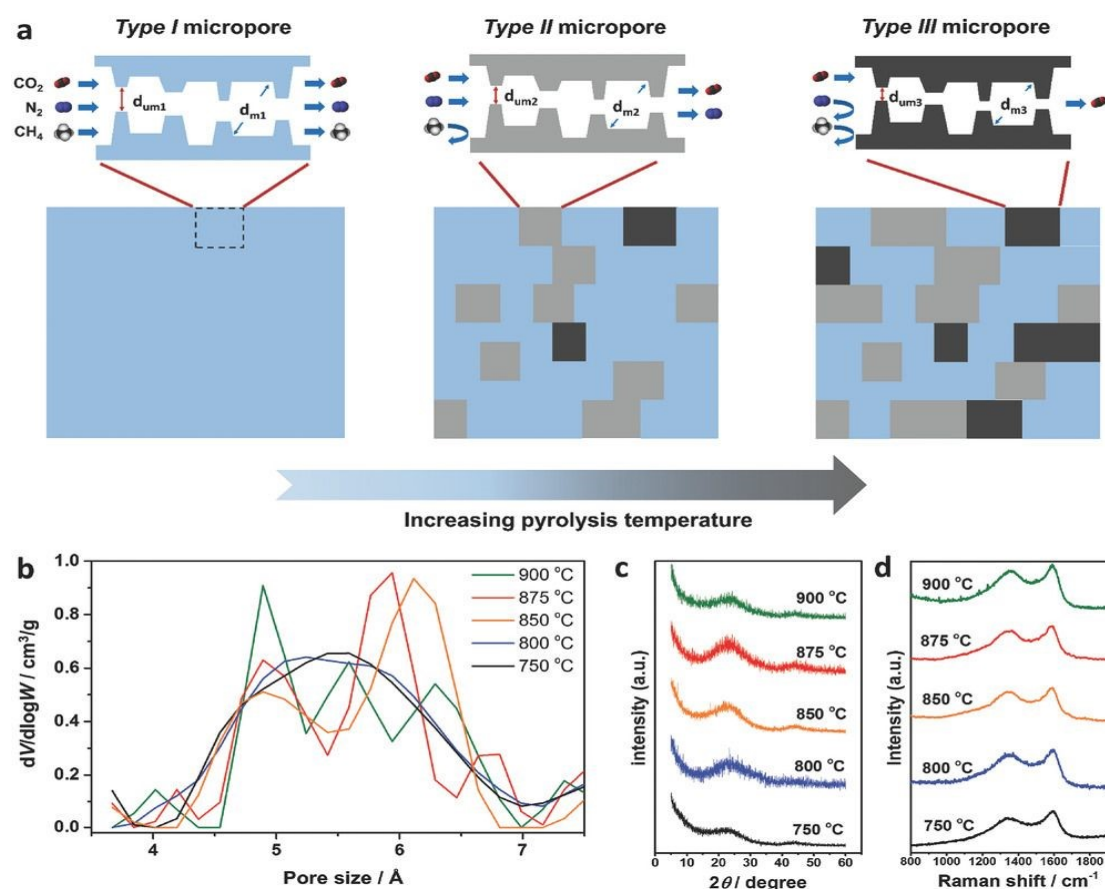


Fig. 9 (a) Structural evolution of carbon/carbon mixed-matrix membranes with pyrolysis temperature (750–900 °C). (b) Pore-size distribution, (c) WAXRD, and (d) Raman spectra of CCMS membranes. Reprinted with permission from ref. 141, Copyright 2017, John Wiley and Sons.

CMS membranes demonstrate unparalleled robustness in extreme conditions. Zhang et al.¹⁴⁶ reported 6FDA/BPDA(1:1)-DAM CMS HFMs maintaining CO₂/CH₄ selectivity ~60 under supercritical natural gas feeds (1800 PSIA, 50% CO₂, 500 ppm C₇ hydrocarbons) across 200 h and -50 to 100 °C thermal cycles. Lei et al.¹⁴⁷ developed cellulose-derived CMS HFMs via ionic liquid spinning, where precursor dried at 140 °C reduced average pore size from 6 to 4.9 Å. Despite a 22% decrease in CO₂ diffusivity, the narrowed pores amplified size exclusion, achieving CO₂/CH₄ ideal selectivity of 917 (2 bar) and mixed-gas separation factor of 131 (50 bar, 60 °C).

Composite CMS membranes represent the future of membrane technology by



enabling tunable separation properties and substantial cost reductions. By integrating economical engineered supports (e.g., P84) with high-performance polymers, precursor hollow fibers with dense skin layers achieve a 25-fold material cost reduction compared to monolithic or ceramic supports. Cao et al.¹⁴⁸ demonstrated this through multi-layer asymmetric CMS HFMs fabricated by coating P84 supports with 6FDA:BPDA-DAM polyimide followed by controlled pyrolysis. Optimizing polymer solution concentration, coating humidity, and pyrolysis temperature yielded CMS-675 membranes with CO₂/CH₄ selectivity of 58.8 and CO₂ permeance of 310 GPU under CO₂/CH₄ (50:50) mixed-gas feed at 35°C. Building on this, Cao et al.¹⁴⁹ developed co-extruded composite CMS membranes using 6FDA-DAM (sheath) and Matrimid® (core), eliminating post-carbonization defect repairs. Pyrolyzed at 675 °C, these membranes achieved enhanced CO₂/CH₄ selectivity of 64.3 and CO₂ permeance of 232 GPU, outperforming single-layer counterparts by 11% in selectivity while maintaining industrial-grade permeance.

4.6 Materials development and transformative pathways

The century-spanning development of hollow fiber membrane materials reflects the balance between permselectivity thresholds, long-term stability, and sustainable manufacturability (Fig. 10, Table S1-S3). Cellulose acetate established the paradigm of bio-sourced membranes yet remains fundamentally constrained by plasticization vulnerabilities; polysulfone delivers exceptional mechanical resilience while undergoing progressive aging-induced performance decay; aromatic polyimides achieve high-precision selectivity through engineered free-volume control, though their intricate synthesis hinders circular economy integration; while thermally rearranged polymers and carbon molecular sieves transcend Robeson upper bounds via tailored ultramicroporosity, their energy-intensive activation processes contradict decarbonization imperatives.

These inherent limitations now drive three transformative innovations: computational materials design integrating multiscale modeling approaches to optimize



the permselectivity-stability-manufacturability trade-offs; bio-hybrid systems integrating enzymatic recycling pathways for closed-loop polymer recovery; and stimuli-responsive membranes featuring dynamically tunable free-volume architectures. This convergence positions next-generation HFMs as adaptive platforms for precision gas separation, where programmable molecular architectures enable autonomous optimization of gas transport across fluctuating natural gas compositions.

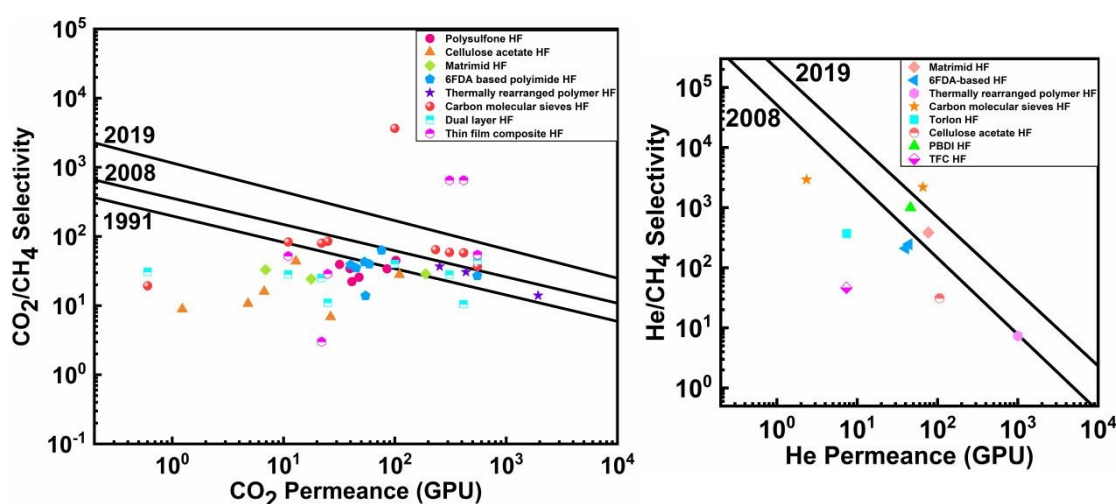


Fig. 10 Gas permeance-selectivity upper bound plots for (a) CO₂/CH₄ and (b) He/CH₄ separation. All evaluated materials assume fabrication with 1 μ m thick selective layers. Benchmark data incorporate state-of-the-art polymeric HFMs, with comprehensive comparisons in Tables S1-S3.

5 HFM performance evaluation

Hollow fiber membranes suffer from three major performance deteriorations: plasticization by penetrant-induced chain mobilization that swells free volume and reduces selectivity; physical aging from gradual free-volume contraction that decreases permeance; and transition-layer collapse originating from capillary forces during phase inversion or pyrolysis stress during carbonization. This section elucidates the underlying mechanisms of these phenomena, links them to performance decline, and analyses stabilization strategies.

5.1 Plasticization

Plasticization in polymeric HFMs refers to the performance degradation caused by



highly soluble components (e.g., CO₂, hydrocarbons) under high-pressure or high-concentration feed streams.^{150, 151} These penetrants act as molecular lubricants, swelling the polymer matrix by increasing inter-chain spacing and segmental mobility, thereby enhancing gas diffusivity while compromising size-sieving selectivity (Fig. 11).^{38, 152, 153} This phenomenon is particularly prevalent in natural gas processing, where CO₂ partial pressures exceed 100 PSIA induce membrane swelling, leading to diminished gas recovery rates and operational reliability.¹⁵⁴⁻¹⁵⁶ Glassy polymers such as 6FDA-based polyimides exhibit dual selectivity mechanisms (diffusivity and solubility-driven), making them promising for CO₂/CH₄ separation.¹⁵⁷ However, their strong CO₂ affinity renders them susceptible to plasticization under mixed-gas conditions, where competitive sorption effects exacerbate performance decline.¹⁵⁸⁻¹⁶⁰ Commercial materials like cellulose acetate and Matrimid® 5218 also face selectivity loss at elevated CO₂ pressures, restricting their application in high-pressure environments.¹⁶¹ The reported plasticization pressure hierarchy for common glassy polymers is: polysulfone (PSf) > polyethersulfone (PES) > P84 > poly(2,6-dimethyl p-phenylene)oxide (PPO) > Matrimid® 5218 (BTDA-DAPI) > cellulose acetate (CA) > cellulose triacetate (CTA).¹⁶² To address this limitation, advanced strategies including cross-linking, post heat-treatment, hydrogen bonding, polymer blending, and semi-interpenetrating polymer networks have been developed for suppressing plasticization.^{158, 163-165}

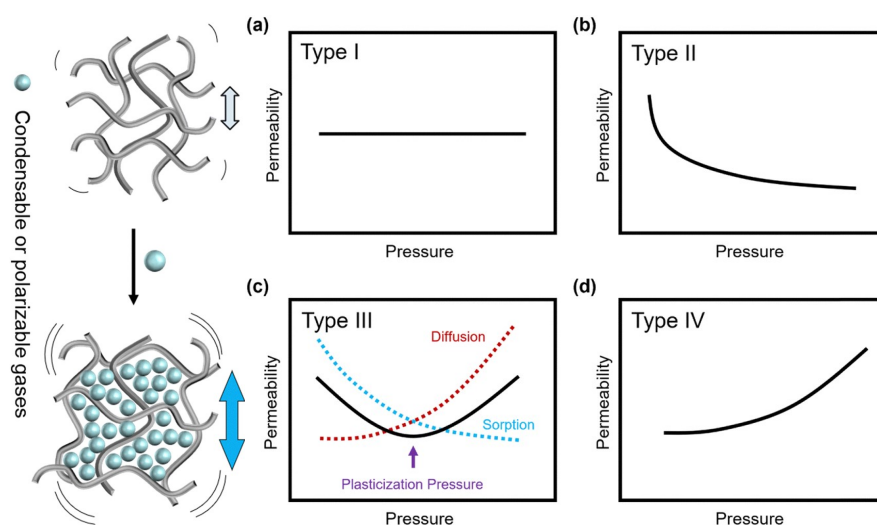


Fig. 11 Schematic illustrating plasticization mechanisms for glassy polymers,



demonstrating four different permeability trends based on varying penetrant behaviors, (a) Non-plasticizing with low sorption, (b) non-plasticizing with moderate sorption, (c) highly sorbing, where the plasticization pressure marks the point at which increased diffusion overcomes the reduction in sorption, and (d) highly plasticizing with very high sorption. Reprinted with permission from ref. 154, copyright 2024, Royal Society of Chemistry.

Chemical crosslinking has emerged as a principal strategy for enhancing plasticization resistance. Five main approaches have been systematically investigated: thermally induced decarboxylation crosslinking, esterification crosslinking, metal ion coordination, amine-mediated nucleophilic crosslinking, and halogen induced radical crosslinking.^{166, 167} Decarboxylation crosslinking forms stable C–C covalent bonds via a decarboxylation-induced free radical reactions that restrict polymer chain mobility while maintaining structural integrity under high feed pressures. Li et al.¹⁶⁸ demonstrated this using 6FDA-mPDA_{0.65}-DABA_{0.3}-TFMB_{0.05} copolyimide HFMs (Fig. 12a-f). Under ternary He/CO₂/CH₄ (0.3/49.5/49.2, v/v/v) feed at 100-600 PSIA, crosslinked HFMs showed minimal permeance variation: He permeance decreased from 13.4 to 9.5 GPU, CH₄ permeance remained stable (0.07-0.08 GPU), and He/CH₄ selectivity declined from 186 to 119. When challenged with hydrocarbon contaminants (propane/heptane), selectivity reductions were limited to 8.7/11.4% at 600 PSIA (Fig. 12g-h), respectively, attributed to crosslinked polymer structure for preventing polymer chain swelling and alleviating competitive adsorption. Wang et al.¹⁶⁹ developed dual thermally crosslinked asymmetric HFMs using 4,4'-diamino-2,2'-biphenyldicarboxylic acid (DCB)-containing copolyimides. The dual crosslinking mechanism combined stable C–C bonds with bulky CF₃ groups from TFMB diamine restricting imide bond rotating, inhibiting transition layer collapse and achieving a skin layer thickness of 1.2 μm. The optimized PI-TFMB-HF@400 membrane demonstrated He permeance of 25 GPU and He/CH₄ selectivity of 269. Under aggressive ternary feed (He/CO₂/CH₄, 0.3/49.7/50, v/v/v), CO₂/CH₄ selectivity decreased by only 24%, while mixed-gas [He/(CO₂+CH₄)] selectivity increased by 80%, showcasing exceptional pressure stability.



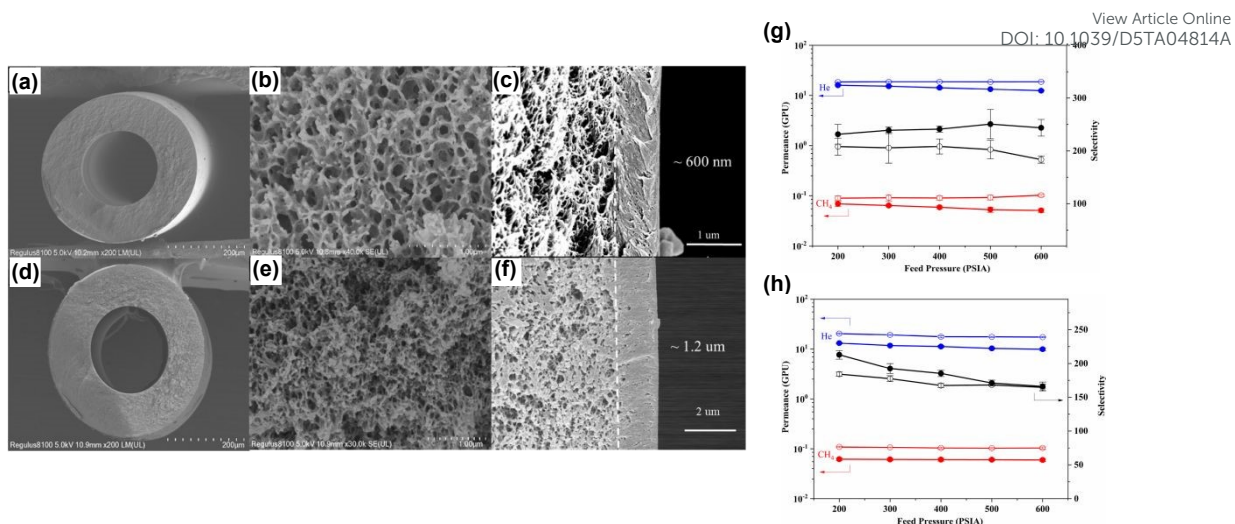


Fig. 12 Structural and performance characterization of crosslinked HFMs. (a-f) SEM images showing preserved substrate porosity and dense skin layer post-crosslinking. Effect of feed pressure on the mixed-gas He and CH₄ permeance and He/CH₄ selectivity of pristine and crosslinked HFMs under ternary (g) He/C₃H₈/CH₄ (0.3/3.0/96.7, v/v/v) and (h) He/n-C₇H₁₆/CH₄ (0.3/0.4/99.3, v/v/v). Reprinted with permission from ref. 166, copyright 2023, Elsevier.

Esterification crosslinking creates robust interchain bridges through transesterification, effectively restricting chain mobility and free volume swelling under high pressure conditions. This significantly enhances plasticization resistance while maintaining size-sieving capabilities. Wallace et al.¹⁷⁰ engineered ester-crosslinked polyimide (6FDA-DAM:DABA 3:2) HFMs, demonstrating that crosslinking temperature more effectively improved plasticization resistance than prolonged treatment duration. The optimized HFMs maintained stable CO₂/CH₄ selectivity of 28 at 1000 PSIA over 100 hours, with full performance recovery at 200 PSIA, indicating reversible swelling without permanent plasticization. Babu et al.¹⁷¹ extended this approach to TEGMC (Triethylene Glycol Monoesterified Crosslinkable) HFMs, achieving H₂S/CH₄ selectivity of 22 under extreme conditions (20% H₂S, 500 PSIA).

To address the risk of transition layer collapse caused by reduced gas permeance in HFMs with ultrathin skin layers, particularly those weakened by thermal crosslinking, Li et al.¹⁷² developed polyimide-cerium (PI-Ce) complex HFMs with a 300 nm ultrathin skin layer made from 6FDA-mPDA_{0.65}-DABA_{0.3}-TFMB_{0.05} copolyimide via

metal ion coordination. This approach enhances plasticization resistance, particularly for helium separation. Under a ternary gas mixture (He/CO₂/CH₄, 0.3/49.4/50.3, v/v/v) at 35 °C and feed pressure ranging from 100 to 600 PSIA, the He permeance of the PI-Ce HFM decreased marginally from 29 to 27 GPU, while CH₄ permeance rose slightly from 0.122 to 0.127 GPU. This led to a 10.8 % decline in He/CH₄ selectivity (239 to 213) as pressure increased from 100 to 400 PSIA. When heavy hydrocarbons (*n*-C₇H₁₆) were introduced, He permeance dropped by 26.3 % (19.8 to 16.5 GPU), and He/CH₄ selectivity decreased by 14.6 % (229 to 194) between 100 and 300 PSIA. The robust plasticization resistance of PI-Ce HFMs highlights their potential for helium recovery in harsh natural gas environments. Liu et al.¹⁷³ incorporated CF₃ groups into polyimide backbones to enhance chain rigidity, producing TFM-PI-CF₃ fibers without skin layer thickening after pyrolysis (200 °C, 2h; Fig. 13a-f). In contrast, the cross-linked TFM-PI-0 fiber showed significantly reduced CO₂ permeance of 46 GPU, 2.5 times lower than its pristine non-cross-linked fiber's permeance of ~115 GPU (Fig. 13g), which is consistent with its increased skin thickness (Fig. 13c-d). Under 55 bar feed gas pressure with 50/50 CO₂/CH₄, these CF₃-modified membranes maintained stable CO₂ permeance (~90 GPU) and selectivity (~43). Even when exposed to 250 ppm hydrocarbon contaminants (heptane/toluene), they retained selectivity > 30 at 55 bar, demonstrating exceptional plasticization resistance (Fig. 13h-i).



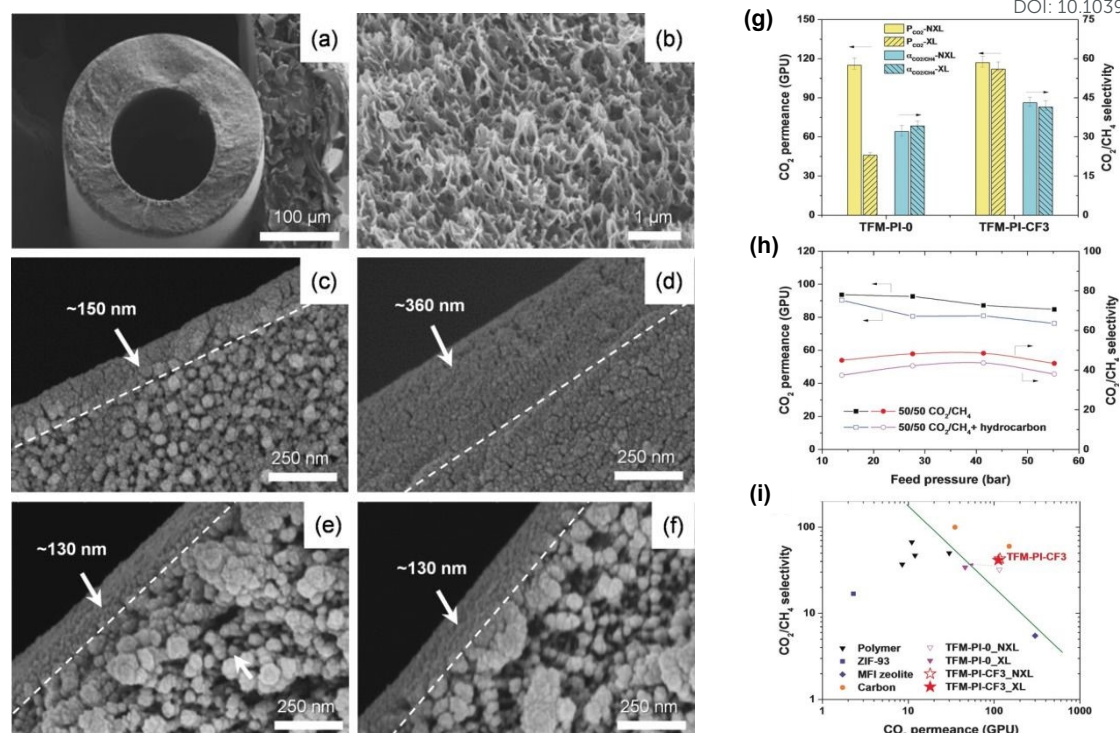


Fig. 13 (a-f) SEM images illustrating CF₃-modified fiber morphology; (g-i) Gas separation performance under hydrocarbon-contaminated high-pressure feeds. Reprinted with permission from ref. 171, copyright 2016, John Wiley and Sons.

For amine-mediated nucleophilic crosslinking, amine-rich agents open imide rings via carbonyl addition, forming amide linkages. Cao et al.¹⁷⁴ demonstrated that immersing 6FDA-2,6-DAT HFMs in *p*-xylenediamine (PXDA)/methanol solution triggers nucleophilic attack on carbonyl groups, generating bis-amide crosslinks. This raised plasticization pressure from 100 PSIA (unmodified and lightly cross-linked) to > 200 PSIA, while stabilizing CO₂ permeance at ~20 GPU. Similarly, Ren et al.¹⁷⁵ demonstrated that PXDA treatment of 6FDA-ODA/NDA HFMs with immersion times exceeding 1.5 min could achieve plasticization resistance up to 550 PSIA (37.4 atm), as confirmed by FTIR analysis showing conversion of imides to amides. This performance marked a substantial enhancement compared to non-crosslinked membranes that plasticized at 75 PSIA.

Thermal annealing, a cost-effective post-treatment, improve membrane stability by increasing packing density, reducing free volume, and elevating glass transition temperature (*T_g*).^{176, 177} Chung et al.¹⁷⁸ thermally treated 6FDA-2,6 DAT HFMs at



250 °C for 5min, minimizing skin layer thickening while suppressing CO₂-induced plasticization. Aged for 60 days, these membranes withstood feed pressures exceeding 500 PSIA, maintaining stable CO₂ permeance of ~34 GPU. This enhanced stability was attributed to tighter chain packing and a denser skin layer. Dong et al.¹⁶² corroborated this by annealing Matrimid® HFMs at 250 °C for 30min, which retained CO₂ permeance near 20 GPU and selectivity of ~28 under CO₂/CH₄ (20/80) mixed-gas at 10-35 bar, showing no plasticization.

Hydrogen bonding has emerged as another strategy to restrict chain mobility and counteract plasticization.⁷¹ Kosuri et al.⁵⁹ fabricated Torlon® HFMs with inter- and intra-chain hydrogen bonds, achieving a CO₂/CH₄ selectivity of 44 (85% of its dense film value of 52). Compared to Ultem® (400 PSIA), Matrimid® (174 PSIA), and 6FDA-DAM:DABA 2:1 (PSIA), Torlon® HFM exhibited superior stability, maintaining constant CO₂ permeance up to 1220 PSIA and a selectivity of 39.6 under supercritical 90% CO₂/10% CH₄ feed. While plasticization typically degrades membrane performance, Liu et al.¹⁶⁵ revealed its benefits for CTA HFMs in aggressive natural gas feeds containing H₂S (20 mol%), light hydrocarbons (C₂H₆: 3 mol%; C₃H₈: 3 mol%), and toluene (300 ppm) at 31.3 bar and 35 °C. Plasticization-induced chain mobility elevated CO₂ and H₂S diffusivity (>110 GPU) while maintaining size-sieving selectivity (22-28 over CH₄). This counterintuitive behavior stems from enhanced condensable gas transport through transient free-volume elements without compromising rigid matrix integrity.



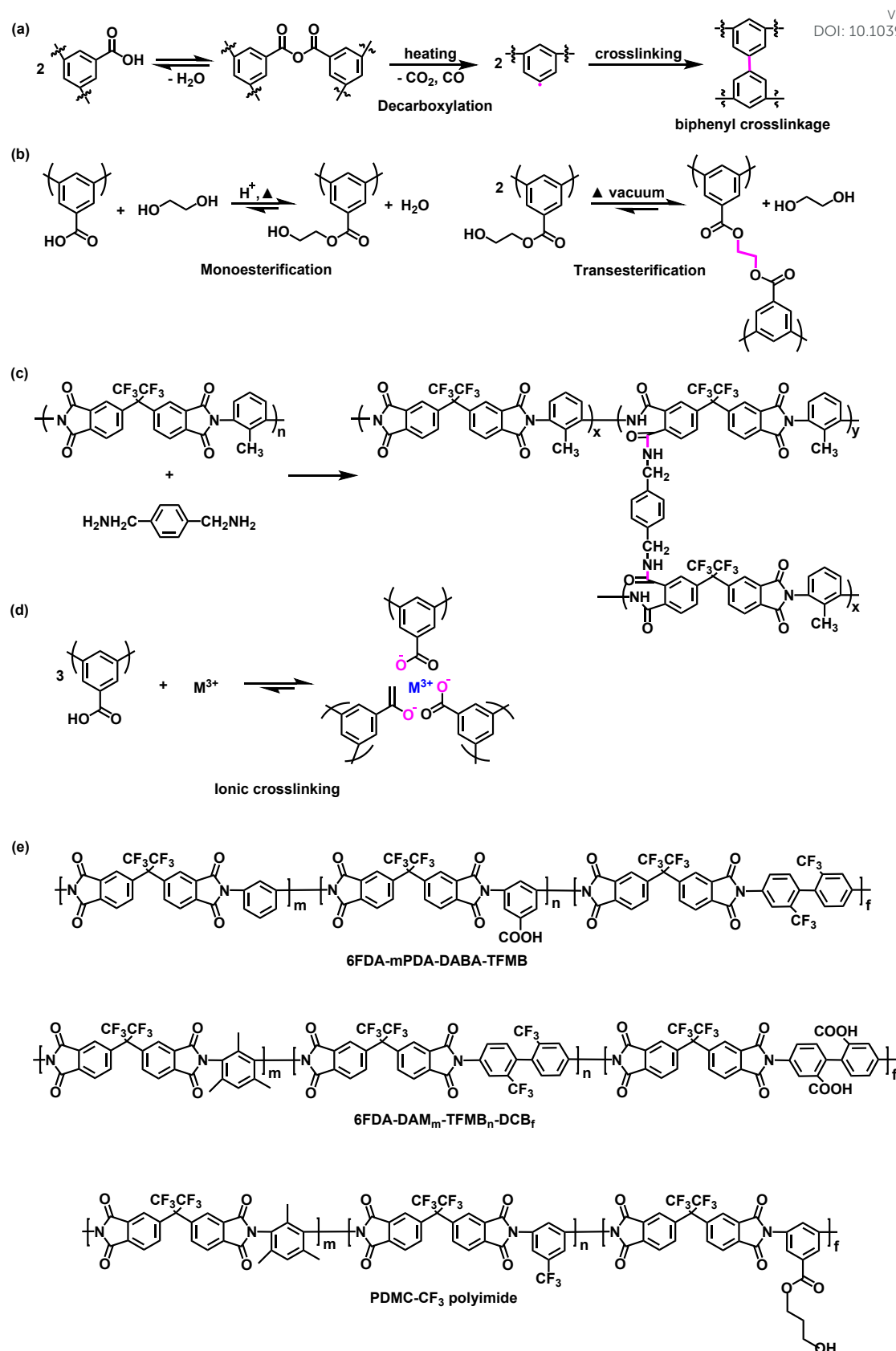


Fig. 14 Summary of strategies for enhancing plasticization resistance in polymer HFMs. Mechanisms include (a) decarboxylation-induced crosslinking, (b) transesterification and ester crosslinking, (c) amine-mediated nucleophilic crosslinking, and (d) ionic



crosslinking. (e) Representative chemical structures of cross-linkable polymers discussed.

5.2 Physical aging

Physical aging describes the gradual structural relaxation of glassy polymers below their glass transition temperature (T_g), where non-equilibrium polymer chains reorganize toward thermodynamic equilibrium.^{155, 179} This densification process reduces excess free volume, leading to declining gas permeance over time (Fig. 15a).¹⁸⁰ During aging, restricted chain mobility elevates the activation energy for gas diffusion (E_D) and diminishes solubility coefficients due to reduced sorption sites availability (Fig. 15b).^{181, 182} Aging kinetics in HFMs are modulated by thermal history ($<1\ \mu\text{m}$ skin layers age faster),^{183, 184} asymmetric architecture (dense skin/porous support),^{185, 186} and processing conditions (e.g., quenching rate).¹⁸⁴⁻¹⁸⁷ Strategies to mitigate physical aging in high-free-volume glassy polymers include CO_2 conditioning, nano-filler incorporation (e.g., MOFs, Mxene, graphene oxide) and structural reinforcement.^{179, 188-192}

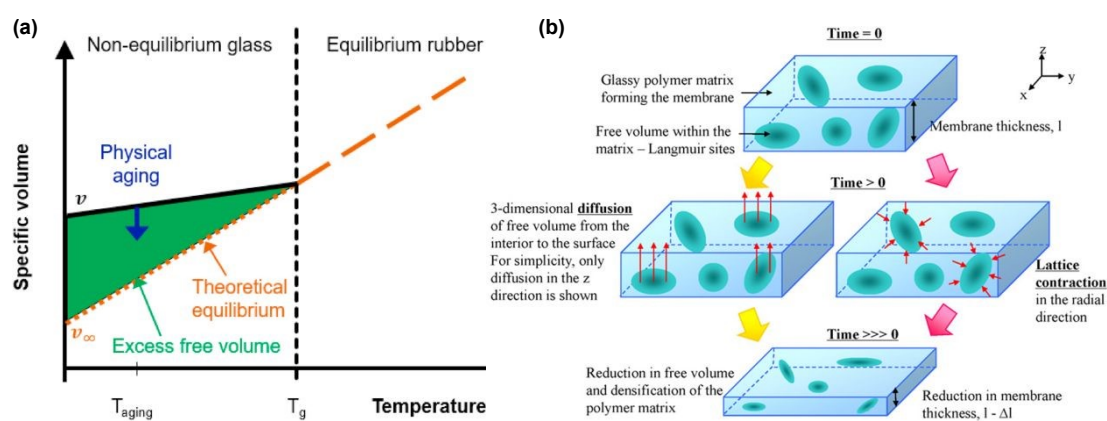


Fig. 15 (a) Specific volume vs. temperature for an amorphous polymer. The extrapolated equilibrium specific volume (dashed line) above T_g diverges from the non-equilibrium state (solid line) below T_g , where excess free volume (green area) becomes kinetically trapped. Physical aging (represented dark blue arrow) indicates the slow relaxation toward equilibrium. Reprinted with permission from ref. 180, copyright 2020, Elsevier. (b) Schematic of free volume diffusion and lattice contraction during aging. Reprinted with permission from ref. 155, copyright 2009, Elsevier.

For instance, Ma et al.¹⁹³ mitigated physical aging of PDMC hollow fiber membrane through CO_2 conditioning and continuous CO_2/CH_4 feed tests. It was found



that periodical 15 PSIG CO₂ conditioning reduced the CO₂ permeance loss of cross-linked HFMs by ~50%, compared to unconditioned ones during a 2300 h aging test. While the HFM exposed to 200 PSIA 50/50 CO₂/CH₄ continuous feed shown a CO₂ permeance loss of only up to 3%, compared the 25% loss for samples without continuous mixed gas feed during a 400 h aging test. These results suggest that physical aging may be essentially quenched as long as the membrane remains contacted with a high CO₂ partial pressure feed typical of actual aggressive feeds for which the membrane would be used. Beyond conditioning strategies, nano-fillers mitigate physical aging by restricting polymer chain relaxation through geometric confinement effects. When incorporated into high-free-volume polymers, the porous/lamellar fillers create tortuous diffusion paths that delay free-volume collapse.^{194, 195} Sutrisna et al.¹⁹⁶ stabilized poly(trimethylsilyl)-1-propyne] (PTMSP) gutter layers using ZIF-8/Pebax-1657 composites coatings. Hydrogen bonding between ZIF-8 ligands and polyamide chains enhanced chain rigidity, while interpenetration of Pebax into PTMSP reduced segmental mobility. The composite membrane maintained stable CO₂ permeance (220~350 GPU) over 15 days at 2 bar, contrasting with bare PTMSP layers, which lost >22% permeance.

Notably, physical aging also impacts CMS HFMs, where the microporous structure undergoes rearrangement over time after pyrolysis.¹⁹⁷ This structural evolution reduces pore accessibility and constricts critical diffusion pathways, leading to substantial declines in gas permeance. Hybridization and surface engineering effectively address this. Shin et al.¹⁹⁸ incorporated ladder-structured poly(phenyl-co-pyridylethyl)silsesquioxane (LPPyr64) into a 6FDA-DAM:DABA (3:2) polyimide before pyrolysis. The rigid siloxane framework preserved the porous microstructure during pyrolysis, yielding CMS fibers with CO₂ permeance of 956 GPU, a 546% increase over precursor fibers (148 GPU). However, untreated CMS PI-LPSQ20 fibers exhibited rapid aging, with CO₂ permeance dropping from 956 to 406.9 GPU within 24 hours post-pyrolysis. PDMS-coated CMS PI-LPSQ20 membranes retained a CO₂



permeance of 354 GPU and CO₂/CH₄ selectivity of 56 after 72 days, with no plasticization observed at 13.2 bar CO₂ partial pressure. Kamath et al.¹⁹⁹ eliminated aging in 6FDA-DETDA: DABA derived CMS by esterifying DABA to DABE and pretreating with 10% vinyltrimethoxysilane (VTMS). This suppressed residual stress-driven rearrangements, stabilizing CO₂ permeance > 1000 GPU for 7 days with a CO₂/CH₄ selectivity of 25 and 780 GPU (selectivity: 48) after 72 days under 21 bar (50 mol% CO₂/CH₄). Synergistic approaches-combining rigid frameworks (LPSQs, MOFs) with polymer backbone engineering and protective coatings (e.g., PDMS)-demonstrate exceptional aging resistance in both polymeric and CMS HFMs.

5.3 Collapse of the nanoporous transition layer

Nanoporous transition layer collapse refers to the densification or structural deformation of the intermediate porous layer between the dense selective skin and the macroporous support in asymmetric HFMs. This phenomenon arises from capillary forces during solvent removal or thermal stresses during high-temperature processing, leading to reduced pore connectivity, thickened skin layers, and diminished gas permeance.^{118, 200} For instance, in the dry/wet phase inversion process, residual solvents with high surface tension (e.g., water) generate significant capillary forces during drying, tightening the pore structure and increasing substructure resistance. Koros et al.¹¹⁸ demonstrated that Matrimid® 5218 HFMs dried directly from water exhibited a skin layer thickness of 1880 nm with a He permeance of only 12.8 GPU. In contrast, solvent-exchanged fibers (using low-surface-tension fluids like hexane) retained a thinner 730 Å skin layer and achieved He permeance of 243.5 GPU, with minimal transition layer collapse. Optimal performance (high selectivity and permeance) was achieved by solvent exchange in methanol followed by hexane prior to drying, highlighting the critical role of solvent selection in membrane morphology and performance.

For CMS HFMs, sub-1 µm skin layers are highly susceptible to transition layer collapse. During pyrolysis, precursor hollow fiber substrates often collapse, resulting in CMS membranes with thick skin layers (15-50 µm).²⁰¹ Pre-treating precursors with



958 silane (e.g., vinyltrimethoxysilane, VTMS) prior to pyrolysis mitigates substrate
 959 collapse, reducing skin thickness to $\sim 3\text{--}6\text{ }\mu\text{m}$, though still thicker than precursor fibers
 960 (Fig. 16b-c).²⁰⁰ To achieve ultrathin skins ($<1\text{ }\mu\text{m}$), Zhang et al.²⁰² developed dual-
 961 layer HFMs combined with silane treatment and in situ hybridization (Fig. 16a). After
 962 hybridization, dual layer ULT CMS-MA1 membranes with a $1\text{ }\mu\text{m}$ skin layer achieved
 963 a CO_2/CH_4 separation factor of $7.9\text{--}36.7$ and CO_2 permeance of $\sim 1,177\text{ GPU}$,
 964 demonstrating effective defect repair. Further optimization reduced the skin layer to $0.5\text{ }\mu\text{m}$
 965 (Fig. 16d-e), yielding CO_2 permeance of $1,452\text{ GPU}$ and CO_2/CH_4 separation factor
 966 of ~ 18 under an equimolar CO_2/CH_4 feed at 100 PSIA and $35\text{ }^\circ\text{C}$. Emerging strategies
 967 such as hierarchical pore structuring, selective silica deposition via silane optimization,
 968 and hybrid precursor designs are critical for scaling these innovations to industrial
 969 applications.

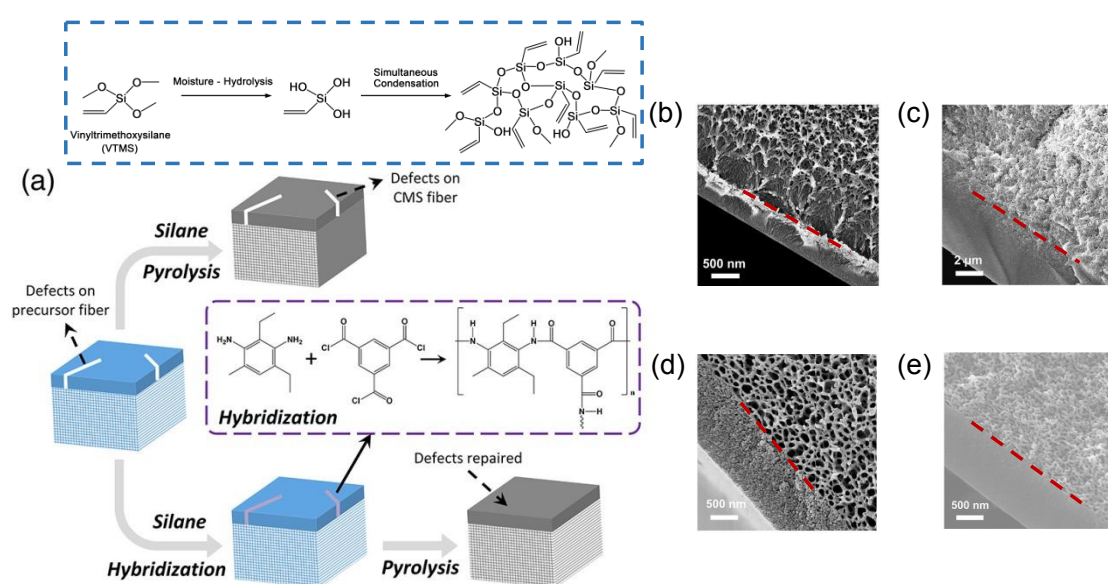


Fig. 16 (a) Schematic of CMS HFM defect repair substrate collapse suppression via silane treatment and in situ hybridization. (b-c) SEM images of monolithic Matrimid® precursor HF and derived CMS HF with silane treatment ($6\text{ }\mu\text{m}$ skin). (d) and (e) SEM images of dual-layer Matrimid®/Matrimid® precursor HF with silane and hybridization treatments, yielding ultrathin ($1\text{ }\mu\text{m}$ skin) CMS HF (ULT CMS MA1). Reprinted with permission from ref. 200, copyright 2019, John Wiley and Sons.

Integrated stabilization strategies empower polymeric hollow fiber membranes to successfully overcome the aforementioned tripartite challenges. Specifically, covalent



crosslinking reinforces polymeric networks through three-dimensional bonding, effectively immobilizing polymer chains to suppress swelling-induced plasticization under CO₂ partial pressures exceeding 500 PSIA. Concurrently, nanoconfined architectures incorporating porous fillers mitigate physical aging by sterically stabilizing interconnected free-volume elements, reducing permeance decay through restricted chain segment relaxation. Complementarily, transition-layer integrity is preserved via optimized solvent-exchange sequences and silane-based interfacial modifications, enabling ultrathin selective skins (<1 μm) with helium permeance sustained. Strategic implementation necessitates balancing chemical resilience against aggressive feed stream, scalable manufacturing viability, and validated operational stability.

6 Conclusion and outlook

This review resolves two fundamental challenges in polymeric hollow fiber membrane technology for sustainable natural gas valorization. First, hierarchical engineering of asymmetric and composite configurations enables precise transport pathway control, achieving efficient helium recovery from sub-0.3% sources and acid gas removal in complex hydrocarbon streams. Second, molecular confinement strategies utilizing covalent stabilization and nanoscale hybridization mitigate aging and plasticization under demanding conditions. Moving forward, three interconnected frontiers are anticipated to shape next-generation HFMs: computational discovery integrating multiscale modeling with machine learning designs advanced polymers possessing adaptive free volume architectures that overcome traditional selectivity-permeance tradeoffs; circular manufacturing adopting enzymatic monomer regeneration and solvent-free processing reduces environmental footprints while enhancing scalability; hybrid membrane systems combining thermally rearranged polymers with carbon molecular sieve supports enable integrated gas refineries capable of simultaneous carbon capture, methane purification, and helium extraction from lean sources. Realizing this vision requires convergent innovations across computational



science, synthetic biology, and modular process engineering to position hollow fiber membranes as intelligent platforms for decarbonized energy infrastructure.

Acknowledgment

The authors would like to extend their sincere gratitude for the financial support received from Shanxi-Zheda Institute of Advanced Materials and Chemical Engineering (2022SZ-TD014), the Project of Stable Support for Youth Team in Basic Research Field in Chinese Academy of Sciences (No. YSBR-017), and National Natural Science Foundation of China (No. 22478396, 22090063).



Reference

- 1 V. Martin-Gil, M. Z. Ahmad, R. Castro-Muñoz and V. Fila, *Sep. Purif. Rev.*, 2018, **48**, 298-324.
- 2 J. B. Powell, *Catal. Today*, 2020, **356**, 27-36.
- 3 *Statistical review of world energy 2024*, Report 73rd edition, Energy Institute, London, 2024.
- 4 X. Chen, G. Liu and W. Jin, *Green Energy Environ.*, 2021, **6**, 176-192.
- 5 Y. Liu, Z. Liu, B. E. Kraftschik, V. P. Babu, N. Bhuvania, D. Chinn and W. J. Koros, *J. Membr. Sci.*, 2021, **632**, 119361.
- 6 C. J. Berganza and J. H. Zhang, *Med. Gas Res*, 2013, **3**, 18.
- 7 A. Cho, *Science*, 2009, **326**, 778-779.
- 8 W. P. Halperin, *Nat. Phys.*, 2014, **10**, 467-470.
- 9 M. Mahesh and P. B. Barker, *J. Am. Coll. Radiol.*, 2016, **13**, 1536-1537.
- 10 R. W. Baker and K. Lokhandwala, *Ind. Eng. Chem. Res.*, 2008, **47**, 2109-2121.
- 11 S. Cavenati, C. A. Grande and A. E. Rodrigues, *Chem. Eng. Sci.*, 2006, **61**, 3893-3906.
- 12 M. Rezakazemi, I. Heydari and Z. Zhang, *J. CO₂ Util.*, 2017, **18**, 362-369.
- 13 R. W. Baker and B. T. Low, *Macromolecules*, 2014, **47**, 6999-7013.
- 14 P. Zheng, W. Xie, Z. Cai, Y. Jiao, Y. Sun, T. Han, X. Ma, N. Li and S. Luo, *J. Membr. Sci.*, 2023, **672**, 121425.
- 15 A. Imtiaz, M. H. D. Othman, A. Jilani, I. U. Khan, R. Kamaludin, J. Iqbal and A. G. Al-Sehemi, *Membranes*, 2022, **12**, 646.
- 16 R. W. Baker, *Ind. Eng. Chem. Res.*, 2002, **41**, 1393-1411.
- 17 G. Li, W. Kujawski, R. Válek and S. Koter, *Int. J. Greenh. Gas. Con.*, 2021, **104**, 103195.
- 18 X. Y. Chen, S. Kaliaguine and D. Rodrigue, *Sep. Purif. Rev.*, 2017, **47**, 66-87.
- 19 C. F. Wan, T. Yang, G. G. Lipscomb, D. J. Stookey and T.-S. Chung, *J. Membr. Sci.*, 2017, **538**, 96-107.
- 20 Y. Huang, C. Xiao, Q. Huang, H. Liu and J. Zhao, *Chem. Eng. J.*, 2021, **403**, 126295.
- 21 C. A. Scholes, G. W. Stevens and S. E. Kentish, *Fuel*, 2012, **96**, 15-28.
- 22 K. Y. Wang, M. Weber and T.-S. Chung, *J. Mater. Chem. A*, 2022, **10**, 8687-8718.
- 23 S. Luo, T. Han, C. Wang, Y. Sun, H. Zhang, R. Guo and S. Zhang, *Ind. Chem. Mater.*, 2023, **1**, 376-387.
- 24 N. Peng, N. Widjojo, P. Sukitpaneemit, M. M. Teoh, G. G. Lipscomb, T.-S. Chung and J.-Y. Lai, *Prog. Polym. Sci.*, 2012, **37**, 1401-1424.
- 25 I. Ullah Khan, M. H. D. Othman, A. F. Ismail, T. Matsuura, H. Hashim, N. A. H. M. Nordin, M. A. Rahman, J. Jaafar and A. Jilani, *J. Nat. Gas Sci. Eng.*, 2018, **52**, 215-234.
- 26 H. S. Lau and W. F. Yong, *J. Mater. Chem. A*, 2021, **9**, 26454-26497.
- 27 R. A. Roslan, W. J. Lau, A. F. Ismail and S. Kartohardjono, *J. Mater. Sci.*, 2024,



- 1058 **59**, 10083-10118.
- 1059 28 S. Shah, J. Liu, S. Ng, S. Luo, R. Guo, C. Cheng and H. Lin, *J. Polym. Sci. Part*
1060 *B Polym. Phys.*, 2016, **54**, 1924-1934.
- 1061 29 Y. Jia, K. Wong, C. Zeng, Liang, J. Wu, T.-S. Chung and S. Zhang, *Prog. Mater.*
1062 *Sci.*, 2024, **146**, 101324.
- 1063 30 C. Arregoitia-Sarabia, D. Gonzalez-Revuelta, M. Fallanza, A. Ortiz and D.
1064 Gorri, *Membranes*, 2022, **12**, 1007.
- 1065 31 L. M. Robeson, *J. Membr. Sci.*, 2008, **320**, 390-400.
- 1066 32 E. P. Favvas, F. K. Katsaros, S. K. Papageorgiou, A. A. Sapalidis and A. C.
1067 Mitropoulos, *React. Funct. Polym.*, 2017, **120**, 104-130.
- 1068 33 J. G. Wijmans and R. W. Baker, *J. Membr. Sci.*, 1995, **107**, 1-21.
- 1069 34 N. Du, H. B. Park, M. M. Dal-Cin and M. D. Guiver, *Energy Environ. Sci.*, 2012,
1070 **5**, 7306-7322.
- 1071 35 H. B. Park, J. Kamcev, L. M. Robeson, M. Elimelech and B. D. Freeman,
1072 *Science*, 2017, **356**, eaab0530.
- 1073 36 M. Wang, J. Zhao, X. Wang, A. Liu and K. K. Gleason, *J. Mater. Chem. A*,
1074 2017, **5**, 8860-8886.
- 1075 37 S. Zhang, *Green Energy Environ.*, 2023, **8**, 1229-1231.
- 1076 38 H. Lin and M. Yavari, *J. Membr. Sci.*, 2015, **475**, 101-109.
- 1077 39 Y. Seo, S. U. Hong and B. S. Lee, *Angew. Chem. Int. Ed.*, 2003, **42**, 1145-1149.
- 1078 40 A. X. Wu, J. A. Drayton and Z. P. Smith, *AIChE J.*, 2019, **65**, e16700.
- 1079 41 A. W. Thornton, T. Hilder, A. J. Hill and J. M. Hill, *J. Membr. Sci.*, 2009, **336**,
1080 101-108.
- 1081 42 T. A. Centeno and A. B. Fuertes, *J. Membr. Sci.*, 1999, **160**, 201-211.
- 1082 43 B. Petrovic, M. Gorbounov and S. M. Soltani, *Micropor. Mesopor. Mater.*, 2021,
1083 **312**, 110751.
- 1084 44 E. R. Gilliland, R. F. Baddour, G. P. Perkinson and K. J. Sladek, *Ind. Eng. Chem.*
1085 *Fundamen.*, 1974, **13**, 95-100.
- 1086 45 P. Pandey and R. Chauhan, *Prog. Polym. Sci.*, 2001, **26**, 853-893.
- 1087 46 S. Higgins, W. DeSisto and D. Ruthven, *Micropor. Mesopor. Mater.*, 2009, **117**,
1088 268-277.
- 1089 47 L. Jiang, T.-S. Chung, D. F. Li, C. Cao and S. Kulprathipanja, *J. Membr. Sci.*,
1090 2004, **240**, 91-103.
- 1091 48 M. Liu, M. D. Nothling, P. A. Webley, Q. Fu and G. G. Qiao, *Acc. Chem. Res.*,
1092 2019, **52**, 1905-1914.
- 1093 49 G. J. Dahe, R. P. Singh, K. W. Dudeck, D. Yang and K. A. Berchtold, *J. Membr.*
1094 *Sci.*, 2019, **577**, 91-103.
- 1095 50 Y. D. Kim, J. Y. Kim, H. K. Lee and S. C. Kim, *J. Membr. Sci.*, 2001, **190**, 69-
1096 77.
- 1097 51 L. Liu, E. S. Sanders, J. R. Johnson, O. Karvan, S. Kulkarni, D. J. Hasse and W.
1098 J. Koros, *J. Membr. Sci.*, 2013, **446**, 433-439.
- 1099 52 Y. Zhang, Y. Chen, X. Hu, B. Cheng and H. Liu, *Macromol. Mater. Eng.*, 2017,



- 1100 **302**, 1700282.
- 1101 53 D. Wang, K. Li and W. K. Teo, *J. Membr. Sci.*, 2002, **208**, 419-426.
- 1102 54 H. Hasbullah, S. Kumbharkar, A. F. Ismail and K. Li, *J. Membr. Sci.*, 2011, **366**,
1103 116-124.
- 1104 55 W. Qiu, L. Liu and W. J. Koros, *J. Membr. Sci.*, 2017, **529**, 150-158.
- 1105 56 D. Wang, W. K. Teo and K. Li, *J. Membr. Sci.*, 2002, **204**, 247-256.
- 1106 57 Z. Li, X. Liu, Y. Sun, L. Gong, C. Liao and S. Luo, *Polymer*, 2025, **323**, 128164.
- 1107 58 L. Liu, Q. Wu, S. Wang, W. Lai, P. Zheng, C. Wang, X. Wei and S. Luo, *Ind.*
1108 *Eng. Chem. Res.*, 2022, **62**, 708-716.
- 1109 59 M. R. Kosuri and W. J. Koros, *J. Membr. Sci.*, 2008, **320**, 65-72.
- 1110 60 W. F. Yong, F. Y. Li, Y. C. Xiao, T. S. Chung and Y. W. Tong, *J. Membr. Sci.*,
1111 2013, **443**, 156-169.
- 1112 61 M. L. Jue, V. Breedveld and R. P. Lively, *J. Membr. Sci.*, 2017, **530**, 33-41.
- 1113 62 T. Hu, G. Dong, H. Li and V. Chen, *J. Membr. Sci.*, 2014, **468**, 107-117.
- 1114 63 X. Ding, Y. Cao, H. Zhao, L. Wang and Q. Yuan, *J. Membr. Sci.*, 2008, **323**,
1115 352-361.
- 1116 64 T. He, M. H. V. Mulder, H. Strathmann and M. Wessling, *J. Membr. Sci.*, 2002,
1117 **207**, 143-156.
- 1118 65 F. Y. Li, Y. Li, T.-S. Chung, H. Chen, Y. C. Jean and S. Kawi, *J. Membr. Sci.*,
1119 2011, **378**, 541-550.
- 1120 66 L. Jiang, *J. Membr. Sci.*, 2004, **240**, 91-103.
- 1121 67 A. Raza, M. Askari, C. Z. Liang, N. Peng, S. Farrukh, A. Hussain and T.-S.
1122 Chung, *J. Membr. Sci.*, 2021, **625**, 119124.
- 1123 68 Y. Li and T.-S. Chung, *J. Membr. Sci.*, 2010, **350**, 226-231.
- 1124 69 Y. Liu, T.-S. Chung, R. Wang, D. F. Li and M. L. Chng, *Ind. Eng. Chem. Res.*,
1125 2003, **42**, 1190-1195.
- 1126 70 C. Ma and W. J. Koros, *Ind. Eng. Chem. Res.*, 2013, **52**, 10495-10505.
- 1127 71 W. Xie, Y. Jiao, Z. Cai, H. Liu, L. Gong, W. Lai, L. Shan and S. Luo, *Sep. Purif.*
1128 *Technol.*, 2022, **282**, 120091.
- 1129 72 A. U. Khan, O. Samuel, M. H. D. Othman, M. Younas, R. Kamaludin, Z. I.
1130 Khan, M. F. A. Al-Ogaili, N. Yoshida, T. A. Kurniawan, M. H. Puteh, F.
1131 Kadir Khan, M. O. Aijaz and M. R. Karim, *J. Environ. Chem. Eng.*, 2025, **13**,
1132 114913.
- 1133 73 G. Li, W. Kujawski, R. Válek and S. Koter, *Int. J. Greenh. Gas Control.*, 2021,
1134 **104**.
- 1135 74 S. Li, Y. Liu, D. A. Wong and J. Yang, *Polymers*, 2021, **13**, 2539.
- 1136 75 L. Liu, A. Chakma and X. Feng, *Ind. Eng. Chem. Res.*, 2005, **44**, 6874-6882.
- 1137 76 W. Lai, L. Liu, J. Bai, L. Xiao, Y. Jiao, Y. Yang, L. Shan and S. Luo, *Chem.*
1138 *Eng. J.*, 2023, **460**, 141708.
- 1139 77 K. C. Khulbe and T. Matsuura, *Polymers*, 2018, **10**, 1051.
- 1140 78 Q. Wu, Y. Jiao, L. Liu, Y. Sun, T. Han, Y. Peng, W. Yang, S. Luo and S. Zhang,
1141 *Chem. Eng. J.*, 2023, **461**, 141976.



- 1142 79 P. Li, H. Z. Chen and T.-S. Chung, *J. Membr. Sci.*, 2013, **434**, 18-25.
- 1143 80 Z. Dai, J. Deng, Q. Yu, R. M. L. Helberg, S. Janakiram, L. Ansaloni and L.
- 1144 Deng, *ACS Appl. Mater.*, 2019, **11**, 10874-10882.
- 1145 81 G. Chowdhury, S. Deng, T. Matsuura and B. Laverty, *J. Appl. Polym. Sci.*, 2001,
- 1146 **79**, 275-282.
- 1147 82 J.-J. Qin and T.-S. Chung, *Desalination*, 2006, **192**, 112-116.
- 1148 83 H. B. Li, W. Y. Shi, J. C. Li and Y. F. Zhang, *Fiber. Polym.*, 2014, **15**, 2553-
- 1149 2563.
- 1150 84 G. V. Theodorakopoulos, D. S. Karousos, K. G. Mansouris, A. A. Sapalidis, E.
- 1151 P. Kouvelos and E. P. Favvas, *Int. J. Greenh. Gas. Con.*, 2022, **114**, 103588.
- 1152 85 S. V. Gutiérrez-Hernández, F. Pardo, A. B. Foster, P. M. Budd, G. Zarca and A.
- 1153 Urtiaga, *Sep. Purif. Technol.*, 2025, **363**, 132254.
- 1154 86 W. Lai, L. Liu, J. Bai, L. Xiao, Y. Jiao, Y. Yang, L. Shan and S. Luo, *Chem.*
- 1155 *Eng. J.*, 2023, **460**.
- 1156 87 E.-S. Jo, X. An, P. G. Ingole, W.-K. Choi, Y.-S. Park and H.-K. Lee, *Chin. J.*
- 1157 *Chem. Eng.*, 2017, **25**, 278-287.
- 1158 88 S.-H. Choi, M. M. B. Sultan, A. A. Alsuwailem and S. M. Zuabi, *Sep. Purif.*
- 1159 *Technol.*, 2019, **222**, 152-161.
- 1160 89 L. Tao, J. He, T. Arbaugh, J. R. McCutcheon and Y. Li, *J. Membr. Sci.*, 2023,
- 1161 **665**, 121131.
- 1162 90 J. Xu, A. Suleiman, G. Liu, R. Zhang, M. Jiang, R. Guo and T. Luo, *Chem.*
- 1163 *Phys. Rev.*, 2024, **5**, 041311.
- 1164 91 F. Mokhtari, Akbar Samadi, A. O. Rashed, X. Li, J. M. Razal, L. Kong, R. J.
- 1165 Varley and S. Zhao, *Prog. Mater. Sci.*, 2025, **148**, 101376.
- 1166 92 I. V. Farr, T. E. Glass, Q. Ji and J. E. McGrath, *High Perform. Polym.*, 2016, **9**,
- 1167 345-352.
- 1168 93 D. F. Sanders, Z. P. Smith, R. Guo, L. M. Robeson, J. E. McGrath, D. R. Paul
- 1169 and B. D. Freeman, *Polymer*, 2013, **54**, 4729-4761.
- 1170 94 J. R. Weidman, S. Luo, J. M. Breier, P. Buckley, P. Gao and R. Guo, *Polymer*,
- 1171 2017, **126**, 314-323.
- 1172 95 Z. Mao, X. Jie, Y. Cao, L. Wang, M. Li and Q. Yuan, *Sep. Purif. Technol.*, 2011,
- 1173 **77**, 179-184.
- 1174 96 Z. Jahan, M. B. K. Niazi, M.-B. Hägg and Ø. W. Gregersen, *J. Membr. Sci.*,
- 1175 2018, **554**, 275-281.
- 1176 97 D. Nikolaeva, I. Azcune, M. Tanczyk, K. Warmuzinski, M. Jaschik, M. Sandru,
- 1177 P. I. Dahl, A. Genua, S. Loïs, E. Sheridan, A. Fuoco and I. F. J. Vankelecom, *J.*
- 1178 *Membr. Sci.*, 2018, **564**, 552-561.
- 1179 98 P. Tanvidkar, B. Nayak and B. V. R. Kuncharam, *J. Polym. Environ.*, 2023, **31**,
- 1180 3404-3417.
- 1181 99 E. SADA, H. KUMAZAWA, J.-S. WANG and M. KOIZUMI, *J. Appl. Polym.*
- 1182 *Sci.*, 1992, **45**, 2181-2186.
- 1183 100 M. M. Rajpure, R. B. Mujmule, U. Kim and H. Kim, *Int. J. Hydrogen Energy*,



- 1184 2024, **50**, 615-628.
- 1185 101 Y.-W. Jeon and M.-S. Shin, *Energy. Procedia.*, 2017, **136**, 219-224.
- 1186 102 N. Sunder, Y.-Y. Fong, M. A. Bustam and W.-J. Lau, *Separations*, 2023, **10**,
1187 41-54.
- 1188 103 S.-H. Pak, Y.-W. Jeon, M.-S. Shin and H. C. Koh, *Environ. Eng. Sci.*, 2016, **33**,
1189 17-24.
- 1190 104 M. Mubashir, Y. F. Yeong, K. K. Lau and T. L. Chew, *Polym. Test.*, 2019, **73**,
1191 1-11.
- 1192 105 M. Mubashir, Y. F. Yeong, T. L. Chew and K. K. Lau, *Sep. Purif. Technol.*,
1193 2019, **215**, 32-43.
- 1194 106 M. Mubashir, Y. Yin fong, C. T. Leng, L. K. Keong and N. Jusoh, *Polym. Test.*,
1195 2020, **81**, 106223.
- 1196 107 A. F. Ismail and W. Lorna, *Sep. Purif. Technol.*, 2003, **30**, 37-46.
- 1197 108 A. J. Erb and D. R. Paul, *J. Membr. Sci.*, 1981, **8**, 11-22.
- 1198 109 A. Naderi, W. F. Yong, Y. Xiao, T.-S. Chung, M. Weber and C. Maletzko,
1199 *Polymer*, 2018, **135**, 76-84.
- 1200 110 R. Guo and J. E. McGrath, in *Polymer Science: A Comprehensive Reference*,
1201 2012, DOI: 10.1016/b978-0-444-53349-4.00153-9, pp. 377-430.
- 1202 111 C. L. Aitken, W. J. Koros and D. R. Paul, *Macromolecules*, 2002, **25**, 3651-
1203 3658.
- 1204 112 W. F. Yong, T.-S. Chung, M. Weber and C. Maletzko, *J. Membr. Sci.*, 2018,
1205 **552**, 305-314.
- 1206 113 X. Liu, B. Cao and P. Li, *Ind. Eng. Chem. Res.*, 2017, **57**, 329-338.
- 1207 114 R. A. Roslan, W. J. Lau, A. K. Zulhairun, P. S. Goh and A. F. Ismail, *J. Polym.*
1208 *Res.*, 2020, **27**, 119-133.
- 1209 115 I. U. Khan, M. H. D. Othman, A. Jilani, A. F. Ismail, H. Hashim, J. Jaafar, A.
1210 K. Zulhairun, M. A. Rahman and G. U. Rehman, *Polym. Test.*, 2020, **84**, 106415.
- 1211 116 B. Sasikumar, S. Bisht, G. Arthanareeswaran, A. F. Ismail and M. H. D. Othman,
1212 *Sep. Purif. Technol.*, 2021, **264**, 118471.
- 1213 117 A. Sharif, H. Koolivand, G. Khanbabaie, M. Hemmati, J. Aalaie, M. R. Kashani
1214 and A. Gheshlaghi, *J. Polym. Res.*, 2012, **19**, 9916.
- 1215 118 D. T. Clausi and W. J. Koros, *J. Membr. Sci.*, 2000, **167**, 79-89.
- 1216 119 Y. Zhuang, J. G. Seong and Y. M. Lee, *Prog. Polym. Sci.*, 2019, **92**, 35-88.
- 1217 120 I. V. Farr, D. Kratzner, T. E. Glass, D. Dunson, Q. Ji and J. E. McGrath, *J.*
1218 *Polym. Sci. Part A Polym. Chem.*, 2000, **38**, 2840-2854.
- 1219 121 X. Chen, S. Kaliaguine and D. Rodrigue, *J. Membr. Sep. Technol.*, 2017, **6**, 1-
1220 15.
- 1221 122 P. Tin, *J. Membr. Sci.*, 2003, **225**, 77-90.
- 1222 123 C. Cao, R. Wang, T. S. Chung and Y. Liu, *J. Membr. Sci.*, 2002, **209**, 309-319.
- 1223 124 S. V. Gutiérrez-Hernández, S. Rico-Martínez, F. Pardo, C. Álvarez, J. A.
1224 Miguel, G. Zarca and A. Urtiaga, *J. Membr. Sci.*, 2024, **698**, 122617.
- 1225 125 H. Hachisuka, T. Ohara and K. Ikeda, *J. Membr. Sci.*, 1996, **116**, 265-272.



- 1226 126 J.-J. Qin, T.-S. Chung, C. Cao and R. H. Vora, *J. Membr. Sci.*, 2005, **250**, 95-103. [View Article Online](#)
DOI: 10.1039/D5TA04814A
- 1227 103.
- 1228 127 L. Xu, C. Zhang, M. Rungta, W. Qiu, J. Liu and W. J. Koros, *J. Membr. Sci.*,
1229 2014, **459**, 223-232.
- 1230 128 J. Lee, J. S. Kim, J. F. Kim, H. J. Jo, H. Park, J. G. Seong and Y. M. Lee, *J.*
1231 *Membr. Sci.*, 2019, **573**, 393-402.
- 1232 129 S. Kim and Y. M. Lee, *J. Nanopart. Res.*, 2012, **14**, 949-960.
- 1233 130 K. T. Woo, J. Lee, G. Dong, J. S. Kim, Y. S. Do, W.-S. Hung, K.-R. Lee, G.
1234 Barbieri, E. Drioli and Y. M. Lee, *J. Membr. Sci.*, 2015, **490**, 129-138.
- 1235 131 K. T. Woo, J. Lee, G. Dong, J. S. Kim, Y. S. Do, H. J. Jo and Y. M. Lee, *J.*
1236 *Membr. Sci.*, 2016, **498**, 125-134.
- 1237 132 K. T. Woo, G. Dong, J. Lee, J. S. Kim, Y. S. Do, W. H. Lee, H. S. Lee and Y.
1238 M. Lee, *J. Membr. Sci.*, 2016, **510**, 472-480.
- 1239 133 J. Lee, J. S. Kim, S.-y. Moon, C. Y. Park, J. F. Kim and Y. M. Lee, *J. Membr.*
1240 *Sci.*, 2020, **595**, 117535.
- 1241 134 S. Kim, S. H. Han and Y. M. Lee, *J. Membr. Sci.*, 2012, **403-404**, 169-178.
- 1242 135 S. Fan, C. Niu, W. Duan, Z. Sun, B. Chen, Z. Ren, J. Wang, G. Tang, G. Zhao,
1243 Y. Liu and P. Li, *J. Membr. Sci.*, 2025, **713**, 123305.
- 1244 136 Y. Jiao, Q. Wu, W. Xu, W. Lai, L. Xiao, X. Mei, H. Zhang and S. Luo, *Sep.*
1245 *Purif. Technol.*, 2023, **315**, 123691.
- 1246 137 C. Zhang, K. Zhang, Y. Cao and W. J. Koros, *Ind. Eng. Chem. Res.*, 2018, **57**,
1247 16051-16058.
- 1248 138 Y. Ma, M. L. Jue, F. Zhang, R. Mathias, H. Y. Jang and R. P. Lively, *Angew.*
1249 *Chem. Int. Ed.*, 2019, **58**, 13259-13265.
- 1250 139 O. Karvan, J. R. Johnson, P. J. Williams and W. J. Koros, *Chem. Eng. Technol.*,
1251 2013, **36**, 53-61.
- 1252 140 G. Liu, Y. Labreche, N. Li, Y. Liu, C. Zhang, S. J. Miller, V. P. Babu, N.
1253 Bhuwania and W. J. Koros, *AIChE J.*, 2019, **65**, 1269-1280.
- 1254 141 YaoMa, M. L. Jue, F. Zhang, R. Mathias, H. Y. Jang and R. P. Lively, *Angew.*
1255 *Chem. Int. Ed.*, 2019, **58**, 13259-13265.
- 1256 142 D. Q. Vu and W. J. Koros, *Ind. Eng. Chem. Res.*, 2002, **41**, 367-380.
- 1257 143 C. Zhang and W. J. Koros, *Adv. Mater.*, 2017, **29**, 1701631.
- 1258 144 M. G. Kamath, A. K. Itta, S. S. Hays, O. Sanyal, Z. Liu and W. J. Koros, *Ind.*
1259 *Eng. Chem. Res.*, 2020, **59**, 13755-13761.
- 1260 145 Q. Wu, L. Liu, Y. Jiao, Z. Y. Li, J. Bai, X. H. Ma, S. J. Luo and S. J. Zhang,
1261 *Angew. Chem. Int. Ed.*, 2024, **63**, e202400688.
- 1262 146 C. Zhang, G. B. Wenz, P. J. Williams, J. M. Mayne, G. Liu and W. J. Koros,
1263 *Ind. Eng. Chem. Res.*, 2017, **56**, 10482-10490.
- 1264 147 L. Lei, A. Lindbråthen, X. Zhang, E. P. Favvas, M. Sandru, M. Hillestad and X.
1265 He, *J. Membr. Sci.*, 2020, **614**, 118529.
- 1266 148 Y. Cao, K. Zhang, O. Sanyal and W. J. Koros, *Angew. Chem. Int. Ed.*, 2019, **58**,
1267 12149-12153.



- 1268 149 Y. Cao, Z. Liu, W. Qiu and W. J. Koros, *Angew. Chem. Int. Ed.*, 2023, **62**, e202303915. View Article Online
DOI: 10.1039/D3TA04814A
- 1269
- 1270 150 K. Tanaka, A. Taguchi, J. Hao, H. Kita and K. Okamoto, *J. Membr. Sci.*, 1996, **121**, 197-207.
- 1271
- 1272 151 K. Okamoto, K. Noborio, H. Jianqiang, K. Tanaka and H. Kita, *J. Membr. Sci.*, 1997, **134**, 171-179.
- 1273
- 1274 152 J. D. Wind, S. M. Sirard, D. R. Paul, P. F. Green, K. P. Johnston and W. J. Koros, *Macromolecules*, 2003, **36**, 6433-6441.
- 1275
- 1276 153 K. Mizrahi Rodriguez, S. Lin, A. X. Wu, K. R. Storme, T. Joo, A. F. Grosz, N. Roy, D. Syar, F. M. Benedetti and Z. P. Smith, *Chem. Soc. Rev.*, 2024, **53**, 2435-2529.
- 1277
- 1278
- 1279 154 L. S. White, T. A. Blinka, H. A. Kloczewski and I. f. Wang, *J. Membr. Sci.*, 1995, **103**, 73-82.
- 1280
- 1281 155 Y. Xiao, B. T. Low, S. S. Hosseini, T. S. Chung and D. R. Paul, *Prog. Polym. Sci.*, 2009, **34**, 561-580.
- 1282
- 1283 156 J. D. Wind, D. R. Paul and W. J. Koros, *J. Membr. Sci.*, 2004, **228**, 227-236.
- 1284 157 C. Cao, *J. Membr. Sci.*, 2003, **216**, 257-268.
- 1285 158 C.-C. Chen, W. Qiu, S. J. Miller and W. J. Koros, *J. Membr. Sci.*, 2011, **382**, 212-221.
- 1286
- 1287 159 T. Rodenas, I. Luz, G. Prieto, B. Seoane, H. Miro, A. Corma, F. Kapteijn, F. X. Llabrés i Xamena and J. Gascon, *Nat. Mater.*, 2014, **14**, 48-55.
- 1288
- 1289 160 J. E. Bachman and J. R. Long, *Energy Environ. Sci.*, 2016, **9**, 2031-2036.
- 1290 161 A. Bos, I. G. M. Pünt, M. Wessling and H. Strathmann, *J. Membr. Sci.*, 1999, **155**, 67-78.
- 1291
- 1292 162 G. Dong, H. Li and V. Chen, *J. Membr. Sci.*, 2011, **369**, 206-220.
- 1293 163 J. Ren, R. Wang, T.-S. Chung, D. F. Li and Y. Liu, *J. Membr. Sci.*, 2003, **222**, 133-147.
- 1294
- 1295 164 W. Qiu, C.-C. Chen, L. Xu, L. Cui, D. R. Paul and W. J. Koros, *Macromolecules*, 2011, **44**, 6046-6056.
- 1296
- 1297 165 Y. Liu, Z. Liu, A. Morisato, N. Bhuvania, D. Chinn and W. J. Koros, *J. Membr. Sci.*, 2020, **601**, 117910.
- 1298
- 1299 166 H. J. Yu, H. An, J. H. Shin, A. Brunetti and J. S. Lee, *Chem. Eng. J.*, 2023, **473**, 145378.
- 1300
- 1301 167 Y. Jiao, Q. Wu, W. Xu, W. Lai, L. Xiao, X. Mei, H. Zhang and S. Luo, *Sep. Purif. Technol.*, 2023, **315**, 123691.
- 1302
- 1303 168 Z. Li, T. Han, W. Lai, J. Ma, Y. Zhang, Q. Wu, C. Wang, C. Liao and S. Luo, *J. Membr. Sci.*, 2023, **688**, 122126.
- 1304
- 1305 169 C. Wang, Z. Li, J. Bai, H. Liu, X. Wang and S. Luo, *Sep. Purif. Technol.*, 2025, **354**.
- 1306
- 1307 170 D. W. Wallace, J. Williams, C. Staudt-Bickel and W. J. Koros, *Polymer*, 2006, **47**, 1207-1216.
- 1308
- 1309 171 V. P. Babu, B. E. Kraftschik and W. J. Koros, *J. Membr. Sci.*, 2018, **558**, 94-



- 1310 105.
- 1311 172 Z. Li, W. Lai, Y. Sun, T. Han, X. Liu, C. Liao and S. Luo, *J. Membr. Sci.*, 2025,
1312 **715**, 123480.
- 1313 173 G. Liu, N. Li, S. J. Miller, D. Kim, S. Yi, Y. Labreche and W. J. Koros, *Angew.
1314 Chem. Int. Ed.*, 2016, **55**, 13754-13758.
- 1315 174 C. Cao, T.-S. Chung, Y. Liu, R. Wang and K. P. Pramoda, *J. Membr. Sci.*, 2003,
1316 **216**, 257-268.
- 1317 175 J. Ren, R. Wang, T.-S. Chung, D. F. Li and Y. Liu, *J. Membr. Sci.*, 2003, **222**,
1318 133-147.
- 1319 176 J. D. Wind, C. Staudt-Bickel, D. R. Paul and W. J. Koros, *Ind. Eng. Chem. Res.*,
1320 2002, **41**, 6139-6148.
- 1321 177 N. Alaslai, B. Ghanem, F. Alghunaimi, E. Litwiller and I. Pinnau, *J. Membr.
1322 Sci.*, 2016, **505**, 100-107.
- 1323 178 T.-S. Chung, J. Ren, R. Wang, D. Li, Y. Liu, K. P. Pramoda, C. Cao and W. W.
1324 Loh, *J. Membr. Sci.*, 2003, **214**, 57-69.
- 1325 179 D. Cangialosi, V. M. Boucher, A. Alegría and J. Colmenero, *Soft Matter*, 2013,
1326 **9**, 8619.
- 1327 180 M. M. Merrick, R. Sujanani and B. D. Freeman, *Polymer*, 2020, **211**, 123176.
- 1328 181 T.-S. Chung and S. Khean Teoh, *J. Membr. Sci.*, 1999, **152**, 175-188.
- 1329 182 W.-H. Lin and T.-S. Chung, *J. Membr. Sci.*, 2001, **186**, 183-193.
- 1330 183 B. W. Rowe, B. D. Freeman and D. R. Paul, *Polymer*, 2009, **50**, 5565-5575.
- 1331 184 B. W. Rowe, B. D. Freeman and D. R. Paul, *Polymer*, 2010, **51**, 3784-3792.
- 1332 185 G. Clarizia, F. Tasselli and P. Bernardo, *Polymers*, 2020, **12**, 441.
- 1333 186 J. Xia, T.-S. Chung and D. R. Paul, *J. Membr. Sci.*, 2014, **450**, 457-468.
- 1334 187 P. H. Pfromm and W. J. Koros, *Polymer*, 1995, **36**, 2379-2387.
- 1335 188 C. Ma and W. J. Koros, *J. Membr. Sci.*, 2018, **551**, 214-221.
- 1336 189 Z.-X. Low, P. M. Budd, N. B. McKeown and D. A. Patterson, *Chem. Rev.*, 2018,
1337 **118**, 5871-5911.
- 1338 190 D. S. Bakhtin, S. E. Sokolov, I. L. Borisov, V. V. Volkov, A. V. Volkov and V.
1339 O. Samoilov, *Membranes*, 2023, **13**, 519.
- 1340 191 Y. Jiao, M. Liu, Q. Wu, P. Zheng, W. Xu, B. Ye, H. Zhang, R. Guo and S. Luo,
1341 *J. Membr. Sci.*, 2023, **672**, 121474.
- 1342 192 Z. Kang, L. Fan and D. Sun, *J. Mater. Chem. A*, 2017, **5**, 10073-10091.
- 1343 193 C. Ma and W. J. Koros, *J. Membr. Sci.*, 2018, **551**, 214-221.
- 1344 194 F. Mokhtari, K. A. S. Usman, J. Zhang, R. Komljenovic, Ž. Simon, B.
1345 Dharmasiri, A. Rezk, P. C. Sherrell, L. C. Henderson, R. J. Varley and J. M.
1346 Razal, *ACS Appl. Mater.*, 2025, **17**, 3214-3228.
- 1347 195 S. M. S. Rana, M. T. Rahman, M. S. Sharma, P. Maharjan, T. Bhatta, H. Cho,
1348 C. Park and J. Y. Park, *ACS Appl. Mater.*, 2021, **13**, 4955-4967.
- 1349 196 P. D. Sutrisna, J. Hou, H. Li, Y. Zhang and V. Chen, *J. Membr. Sci.*, 2017, **524**,
1350 266-279.
- 1351 197 X. He, J. A. Lie, E. Sheridan and M.-B. Hägg, *Ind. Eng. Chem. Res.*, 2011, **50**,



View Article Online
DOI: 10.1039/D5TA04814A

- 1352 2080-2087.
- 1353 198 J. H. Shin, H. J. Yu, H. An, A. S. Lee, S. S. Hwang, S. Y. Lee and J. S. Lee, *J.*
1354 *Membr. Sci.*, 2019, **570-571**, 504-512.
- 1355 199 M. G. Kamath, S. Fu, A. K. Itta, W. Qiu, G. Liu, R. Swaidan and W. J. Koros,
1356 *J. Membr. Sci.*, 2018, **546**, 197-205.
- 1357 200 N. Bhuvania, Y. Labreche, C. S. K. Achoundong, J. Baltazar, S. K. Burgess, S.
1358 Karwa, L. Xu, C. L. Henderson, P. J. Williams and W. J. Koros, *Carbon*, 2014,
1359 **76**, 417-434.
- 1360 201 L. Xu, M. Rungta and W. J. Koros, *J. Membr. Sci.*, 2011, **380**, 138-147.
- 1361 202 C. Zhang, R. Kumar and W. J. Koros, *AIChE J.*, 2019, **65**, e16611.
- 1362



Data Availability Statement

The data supporting this review article are derived from published studies cited throughout the manuscript. All referenced datasets and experimental results are available in the original publications, as indicated in the reference list. No new primary data were generated for this review. For further details, readers are directed to the corresponding references or may contact the authors for specific inquiries.

